arXiv:1601.02985v1 [astro-ph.GA] 12 Jan 2016

Interstellar Hydrides

Maryvonne Gerin,[1,2] David A. Neufeld,[3,4] and Javier R. Goicoechea[5]

[1]LERMA, Observatoire de Paris, PSL Research University, CNRS, UMR8112,Paris, France, F-75014, Paris, email:maryvonne.gerin@ens.fr
[2]Sorbonne Universités, UPMC Univ. Paris 06, UMR8112, LERMA, Paris, France, F-75005
[3]Department of Physics and Astronomy, The Johns Hopkins University, Baltimore, USA, MD 21218, email : neufeld@jhu.edu
[4]Visiting Professor, Astronomy Department, University of Maryland, College Park, USA, MD20742
[5]Grupo de Astrofísica Molecular, Instituto de Ciencia de Materiales de Madrid (CSIC). E-28049. Madrid, Spain. email: jr.goicoechea@icmm.csic.es

Xxxx. Xxx. Xxx. Xxx. 2016. 54:1–43

This article's doi:
10.1146/((please add article doi))

Copyright © 2016 by Annual Reviews.
All rights reserved

Keywords

Interstellar medium, Interstellar molecules, Molecular ions, Astrochemistry, Molecular spectroscopy

Abstract

Interstellar hydrides – that is, molecules containing a single heavy element atom with one or more hydrogen atoms – were among the first molecules detected outside the solar system. They lie at the root of interstellar chemistry, being among the first species to form in initially-atomic gas, along with molecular hydrogen and its associated ions. Because the chemical pathways leading to the formation of interstellar hydrides are relatively simple, the analysis of the observed abundances is relatively straightforward and provides key information about the environments where hydrides are found. Recent years have seen rapid progress in our understanding of interstellar hydrides, thanks largely to far-IR and submillimeter observations performed with the *Herschel* Space Observatory. In this review, we will discuss observations of interstellar hydrides, along with the advanced modeling approaches that have been used to interpret them, and the unique information that has thereby been obtained.

Contents

1. INTRODUCTION 2
   1.1. Historical perspective 2
   1.2. Thermochemistry of interstellar hydrides 5
   1.3. Excitation of interstellar hydrides 7
2. CHEMISTRY 8
   2.1. Gas phase processes 8
   2.2. Solid phase processes 11
3. HYDRIDES IN DIFFUSE GAS 12
   3.1. Overview 12
   3.2. Optical/UV and centimeter-wavelength observations of interstellar hydrides 12
   3.3. FIR and submillimeter observations of absorption by interstellar hydrides 13
4. HYDRIDES IN DENSE, STRONGLY UV-IRRADIATED GAS 16
   4.1. The role of vibrationally excited H_2 in the chemistry 16
   4.2. Oxygen hydrides 18
   4.3. Formation pumping and the excitation of reactive hydride ions 19
5. HYDRIDES IN SHOCKS AND TURBULENT DISSIPATION REGIONS 20
   5.1. Shocks 20
   5.2. Turbulent dissipation regions 23
6. HYDRIDES IN DENSE AND SHIELDED GAS 24
   6.1. Water and oxygen hydrides 25
   6.2. Methane and carbon hydrides 26
   6.3. Ammonia and nitrogen hydrides 27
   6.4. Sulfur and other heavy element hydrides 29
7. HYDRIDES AS DIAGNOSTIC TOOLS 29
   7.1. Hydride as tracers of H_2 30
   7.2. Probes of the molecular fraction 32
   7.3. Probes of the cosmic-ray ionization rate 32
   7.4. Other diagnostic uses 33
8. HYDRIDES IN EXTERNAL GALAXIES 34
   8.1. Local galaxies 34
   8.2. Active Galactic Nuclei : XDR prototypes 35
   8.3. High redshift galaxies 35
9. CONCLUSIONS AND FUTURE PROSPECTS 36

1. INTRODUCTION

1.1. Historical perspective

Although dust and gas clouds were suspected to exist early in the 20th century, the survival of molecules in the harsh ISM was more controversial (e.g. Eddington 1926). Together with CN, the hydrides CH and CH^+ were the first gas-phase molecules detected in the 1930's and 1940's (e.g. Swings & Rosenfeld 1937; Douglas & Herzberg 1941). The improved spectral resolution of visible light spectrometers allowed the detection of very narrow absorption lines in the spectra obtained towards nearby and bright stars. Their associated wavelengths were well known to molecular spectroscopists and the small line-widths suggested low gas temperatures, much lower than those of the stellar atmospheres producing broad atomic features. Indeed, the observed narrow lines remained stationary in the spectra of spectroscopic binary stars whose photospheric lines showed periodic ve-

locity shifts. Thus they were attributed to foreground interstellar clouds (today associated with diffuse clouds with gas densities, defined as n_H=n(H)+2n(H_2), of less than a few hundred hydrogen atoms per cm^3 and gas kinetic temperatures, T, of about 100 K). The interpretation of these pioneering hydride detections was not obvious. Early attempts to model the formation of CH and CH^+ focused on the slow radiative association of C^+ and C with hydrogen atoms (Kramers & Ter Haar 1946). Chemical reactions with H_2 were ignored just because they were known to be endothermic, and because interstellar H_2 was not even detected. It was also suggested that molecules such as CH^+ could be a dissociation product of CH_4 sublimated from grains near stars (Bates & Spitzer 1951). Both atomic and molecular hydrogen were discovered later in the cold neutral medium (CNM), HI at 1420 MHz by radio techniques in the 1950's (Ewen & Purcell 1951), and H_2 twenty years later by electronic absorption lines in the FUV from sounding rockets and from *Copernicus* satellite observations (e.g. Carruthers 1970a; Spitzer et al. 1973).

ISM: Interstellar Medium

Millimeter- and radio-frequency searches for rotational and lambda-type doubling emissions were also recognized as a promising method for detecting new interstellar molecules, for example by Townes (1957), who presented predictions for the frequencies of several key transitions. These early line frequency predictions contributed to the development of radio astronomy in the cm domain and led to the first detection of OH at 1.7 GHz (Weinreb et al. 1963), NH_3 at 23 GHz (the first polyatomic molecule in space, Cheung et al. 1968) and H_2O at 22 GHz (Cheung et al. 1969). OH was also the first molecule detected outside the Milky Way (Weliachew 1971). NH_3 and H_2O were discovered by the team of Nobel Prize winner C.H. Townes. Most of the subsequent discoveries of new molecules required the development of higher frequency heterodyne receivers in the mm and submm domains available from ground-based telescopes (e.g., Falgarone, Phillips & Pearson 2005), and more recently in the far-infrared (FIR), a wavelength region that is only available from stratospheric and space observations (e.g., Gerin et al. 2012, and references therein). These techniques allow the detection of pure rotational transitions at very high spectral resolution (less than 1 km s^{-1}); thus fine and hyperfine line splittings can be resolved. In addition, the FIR domain allows the detection of rotationally excited emission lines. This permits high temperature and density environments (T>100 K and n_H>10^4 cm^{-3}), such as those in star forming regions, to be probed. In diffuse and translucent clouds, hydrides such as CH^+, CH, HCl, NH, OH, OH^+ or SH can be nowadays also studied through their electronic absorption bands in the UV-visible domain at velocity resolutions of a few km s^{-1} (e.g., Federman et al. 1995; Krełowski, Beletsky & Galazutdinov 2010; Zhao et al. 2015). NH in particular, was first detected in this domain (Meyer & Roth 1991). In dense but cold clouds (T≃20 K), hydrides also exist in the solid-phase as ice mantles covering dust grains (see the review by Boogert, Gerakines & Whittet 2015). Their vibrational modes can be detected in the IR domain. The first mantles detected in absorption were water and ammonia ices (Merrill, Russell & Soifer 1976). Table 1 shows a compilation of the detected hydrides and the wavelength range in which they have been observed.

FUV: Far ultraviolet, defined as the 91.2 to 200 nm wavelength region, corresponding to photon energies between 6 and 13.6 eV

FIR: Far infrared, defined as the 20 to 300μm wavelength region, corresponding to frequencies between 1 and 15 THz.

The formation of H_2 on grain surfaces rather than in the gas-phase was soon established, and first models suggested that most hydrogen should be molecular at visual extinctions A_V>1.5 mag (e.g., Hollenbach, Werner & Salpeter 1971). Other molecules were proposed to form on grains as well (Watson & Salpeter 1972). More complete chemical models of diffuse clouds were developed (Solomon & Klemperer 1972; Black & Dalgarno 1977). The chemistry of molecular cloud interiors (most hydrogen in H_2) was also modeled and predicted to be dominated by ion-molecule reactions maintained by cosmic-ray particle ionization (Herbst & Klemperer 1973). These chemical models were the basis of more sophisticated diffuse cloud, dense photodissociation region (PDR), shock and turbulence dissipation models developed later in the 1980's. Supported by laboratory and theoretical studies, these models were also critical in predicting the existence of new hydride molecules in space. Review articles have been presented previously by van Dishoeck (1998) and Snow & McCall (2006)

Table 1 Main astrophysical hydrides[a)]

Formula	Name	Spectral domain[b)]	Ref.
H_2	Molecular Hydrogen	UV-Visible, IR, FIR	Carruthers (1970b)
H_3^+	Protonated molecular hydrogen	IR	Geballe & Oka (1996)
CH	Methylidyne	UV-Visible, (sub)mm, cm	Swings & Rosenfeld (1937)
CH_2	Methylene	FIR, (sub)mm	Hollis, Jewell & Lovas (1995)
CH_3	Methyl	IR	Feuchtgruber et al. (2000)
CH_4	Methane	IR	Lacy et al. (1991)
CH^+	Methylidynium	UV-Visible, FIR, (sub)mm	Douglas & Herzberg (1941)
CH_3^+	Methylium	IR, (sub)mm	Roueff et al. (2013)[c]
NH	Imidogen	UV-Visible, (sub)mm	Meyer & Roth (1991)
NH_2	Amidogen	(sub)mm	van Dishoeck et al. (1993)
NH_3	Ammonia	(sub)mm, cm	Cheung et al. (1968)
NH_4^+	Ammonium	(sub)mm	Cernicharo et al. (2013)[d)]
OH	Hydroxyl radical	UV-Visible, FIR, cm	Weinreb et al. (1963)
H_2O	Water	FIR, (sub)mm, cm	Cheung et al. (1969)
OH^+	Hydroxylium	UV-Visible, (sub)mm	Wyrowski et al. (2010)
H_2O^+	Oxidaniumyl	UV-Visible, (sub)mm	Ossenkopf et al. (2010)
H_3O^+	Hydronium	FIR, (sub)mm	Phillips, van Dishoeck & Keene (1992)
HF	Hydrogen fluoride	FIR	Neufeld et al. (1997)
SH	Mercapto radical	UV-visible, FIR	Neufeld et al. (2012)
H_2S	Hydrogen sulfide	(sub)mm	Thaddeus et al. (1972)
SH^+	Sulfanylium	(sub)mm	Benz et al. (2010); Menten et al. (2011)
HCl	Hydrogen chloride	UV-visible, (sub)mm	Blake, Keene & Phillips (1985)
HCl^+	Chloroniumyl	FIR	De Luca et al. (2012)
H_2Cl^+	Chloronium	(sub)mm	Lis et al. (2010a)
ArH^+	Argonium	(sub)mm	Barlow et al. (2013)

[a)] Adapted from The Astrochymist (www.astrochymist.org); [b)] The corresponding wavelength ranges are : UV-Visible 100 – 1000nm, IR : 1 – 20 μm, FIR 20 – 300 μm ; (sub)mm 0.3 – 4 mm; cm 1 - 20 cm; [c)] A tentative detection of the isotopologue CH_2D^+ is reported; [d)] The detection of the isotopologue NH_3D^+ is reported.

on diffuse interstellar clouds, by Hollenbach & Tielens (1999) on PDRs, and by Bergin & Tafalla (2007) and Caselli & Ceccarelli (2012) for dark clouds.

Recent years have seen rapid progress in our understanding of interstellar hydrides, with new detections and modeling approaches demonstrating their diagnostic power. Thus it seems appropriate to review the current state of observations in different interstellar environments, and the unique astrophysical information that can be obtained. This review is organized as follows. After a general introduction of the thermochemical properties and of the excitation of hydrides, in Section 2 we summarize the main gas-phase and solid-phase processes driving the chemistry of hydrides. We then focus on the appearance of hydride molecules in the diffuse molecular gas (Section 3), in dense and strongly UV-irradiated gas (Section 4), in shocks and turbulent dissipation regions (Section 5), and in cold and dense gas shielded from UV radiation (Section 6). In Section 7 we summarize the diagnostic power of hydrides, and in Section 8 we extend our discussion to external galaxies. We end by giving our conclusions and anticipating some of the exciting prospects for hydride research for the years to come.

PDR:
Photo-Dissociation Region

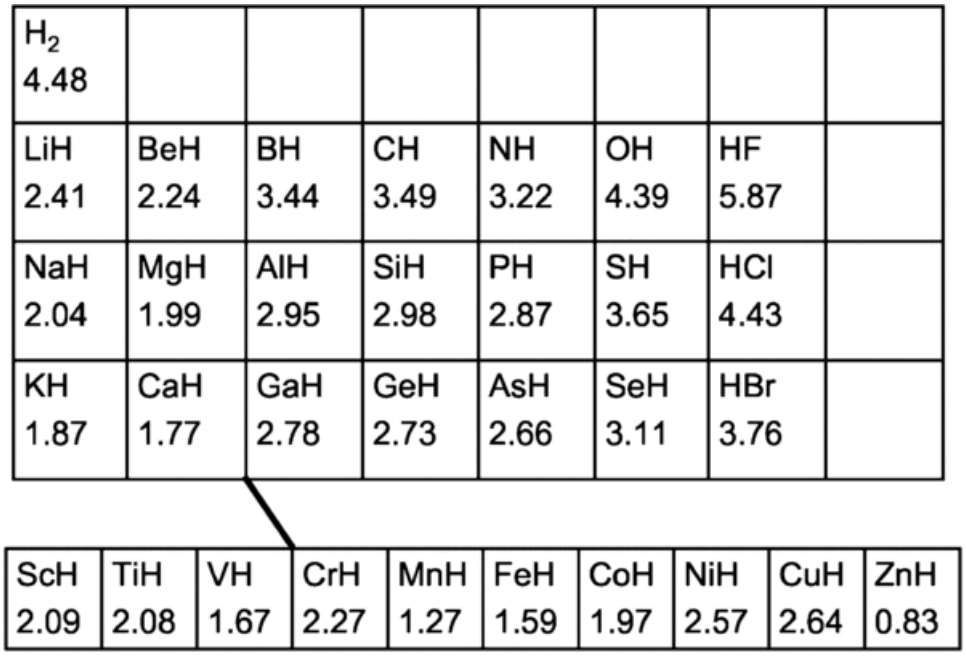

Figure 1

Dissociation energies of the neutral diatomic hydrides, in eV, from Neufeld & Wolfire (2009) and based upon the thermochemical data referenced therein.

1.2. Thermochemistry of interstellar hydrides

Although the interstellar gas is far from thermochemical equilibrium, key features of the chemistry of interstellar hydrides – discussed in detail in Section 2 below – are determined by thermochemistry (Neufeld & Wolfire 2009). Among the elements in the second and third rows of the periodic table, F, O, N, Ne and Ar all have first ionization potentials greater than that of atomic hydrogen (13.60 eV); because hydrogen atoms shield them very effectively from ultraviolet radiation of sufficient energy to ionize them, these elements are predominantly neutral in the CNM. All other elements in the second and third rows of the periodic table – including C, Si, P, S and Cl – have ionization potentials smaller than that of hydrogen; typically, they are predominantly singly-ionized in the cold diffuse ISM. (The exception is Cl, which may exhibit a significant neutral fraction in clouds with a sufficient H_2 fraction: this behavior is a consequence of the rapid reaction of Cl^+ with H_2 to form HCl^+, which subsequently undergoes dissociative recombination to form atomic chlorine).

CNM: Cold Neutral Medium. Two neutral phases coexist at pressure equilibrium in the ISM, the warm neutral medium with $T \sim 10^4$ K and $n_H \sim 0.3 - 1\,cm^{-3}$ and the CNM with $T \sim 10^2$ K and $n_H \sim 30 - 100\,cm^{-3}$.

With the notable exception of hydrogen fluoride, every neutral diatomic hydride has a dissociation energy smaller than that of H_2, as indicated in **Figure 1**. As a result, hydrogen abstraction reactions of the type $X + H_2 \rightarrow XH + H$ are all endothermic except in the case where X is fluorine. HF is therefore the only neutral diatomic hydride that can be formed at low temperature through the reaction of an atom with H_2. As for the diatomic hydride *cations*, HeH^+, OH^+, HF^+, HCl^+, ArH^+ and NeH^+ have dissociation energies larger than that of H_2. They can therefore be produced exothermically[1] via the hydrogen abstraction reaction $X^+ + H_2 \rightarrow XH^+ + H$; such reactions are endothermic for all other ions

[1]For Ne^+ and He^+, the alternative reaction channel to $X + H + H^+$ is also exothermic and is favored.

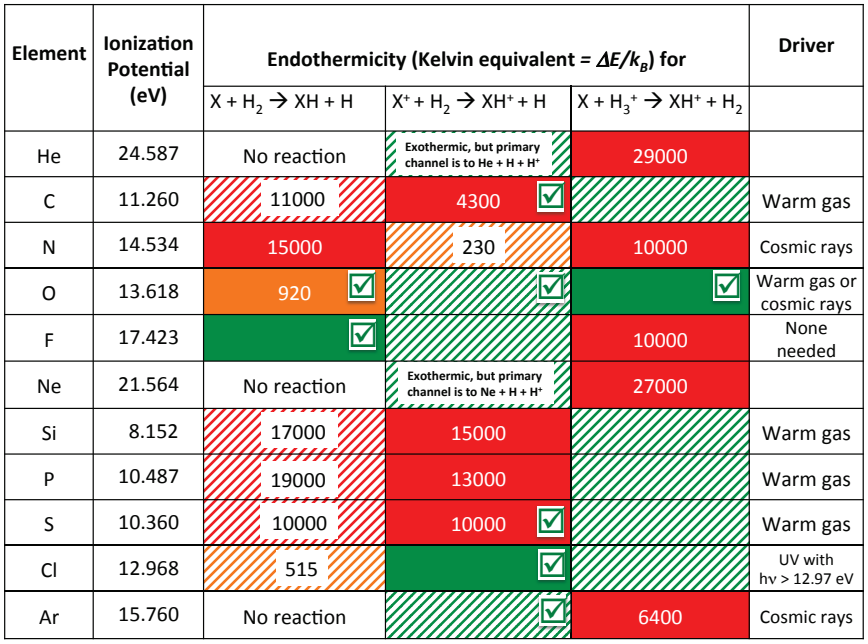

Figure 2

Ionization potentials for selected elements, and endothermicities of three key reactions of possible importance in the formation of interstellar hydrides. See text for a complete description. As indicated in Table 1, CH, CH^+, NH, OH, OH^+, HF, SH, SH^+, HCl, HCl^+ and ArH^+ have been detected in the ISM.

XH^+.

In addition to the ionization potential of each atom, X, and the dissociation energies of the hydrides, XH and XH^+, another important thermochemical parameter is the proton affinity of X. Because H_3^+ is produced efficiently following cosmic-ray ionization of H_2, proton transfer from H_3^+ can be an important production mechanism for XH^+ when the proton affinity of X exceeds that of H_2 (422.3 kJ mol^{-1} or equivalently 4.38 eV). This condition is satisfied for C, O, Si, P, S and Cl – but not for N, F, Ne or Ar – with the result that the first six atoms can react exothermically with H_3^+ to form XH^+. This consideration is most important for O, because it is the only atom among these six to be predominantly neutral in diffuse clouds.

In **Figure 2**, the thermochemical considerations discussed above are presented in graphical form. For each element, the first ionization potential is given in the second column from the left. The 3rd, 4th, and 5th columns indicate the endothermicity of three key reactions: the reaction of X with H_2 to form XH, the reaction of X^+ with H_2 to form XH^+, and the reaction of X with H_3^+ to form XH^+. Here, the endothermicities, ΔE, are presented as temperatures, $\Delta E/k_B$, and given in units of Kelvin. Cells shown in green indicate exothermic reactions, those shown in orange indicate slightly endothermic reactions with $\Delta E/k_B \leq 1000$ K, and those shown in red indicate endothermic reactions with $\Delta E/k_B \geq 1000$ K. Particularly for neutral-neutral reactions, the activation energy (i.e. energy barrier) may exceed the endothermicity. For example, the reaction of O with H_2 to form OH and H has an endothermicity, $\Delta E/k_B \sim 920$ K but an activation energy of $\Delta E_A/k_B \sim 3000$ K. Where the reactant (X

or X^+) is the dominant ionization state of the element in diffuse interstellar gas clouds with a small molecular fraction, the green, orange or red coloring is solid; otherwise, the cell is shaded. The dominant production mechanisms for diatomic interstellar hydrides, and the environments in which they are found, can largely be inferred from the information presented in this matrix. Check marks indicate reactions that have been invoked as significant production routes in astrochemical models in the literature. In some cases, different mechanisms are important in different environments: in the case of oxygen for example, production of OH via the endothermic reaction of O and H_2 becomes rapid in warm ($T \geq 400$ K) gas (e.g. Kaufman & Neufeld 1996), while OH^+ production is effective in cold diffuse gas through reaction of O^+ with H_2 or (in slightly denser gas with a larger H_2 fraction) of O with H_3^+ (e.g. Hollenbach et al. 2012).

1.3. Excitation of interstellar hydrides

Several physical processes determine the excitation of interstellar hydrides (e.g. Roueff & Lique 2013, and references therein), including collisional excitation, spontaneous radiative decay, radiative excitation, and formation pumping. At sufficiently high densities, the first of these processes drives the molecular excitation to local thermodynamic equilibrium (LTE), in which the relative level populations are given by Boltzmann factors determined by the gas kinetic temperature. However, the "critical density" needed to achieve LTE is typically larger for the rotational states of hydrides than that for those of non-hydride interstellar molecules, because hydrides have smaller momenta of inertia, larger rotational constants, and much larger spontaneous radiative rates (the latter scaling as the cube of the transition frequency for a given dipole matrix element). At densities below the critical density, the level populations reach a quasi-equilibrium in which the total production and loss rates are equal for every state. In general, the excitation is "sub-thermal," with the excitation temperatures for most transitions being smaller than the gas kinetic temperature. However, specific transitions can sometimes be supra-thermally-excited, or even inverted, giving rise to maser amplification.

LTE: Local Thermodynamic Equilibrium, where the level populations of a given molecule are determined by Boltzmann equilibrium at the local kinetic temperature, T.

critical density: The density at which the rate of collisional de-excitation from a given state is equal to the rate of spontaneous radiative decay.

In diffuse molecular clouds, the molecular excitation is often determined primarily by the radiation field; in clouds that are not close to a strong submillimeter radiation source, the cosmic microwave background radiation (CMB) dominates and most rotational transitions have an excitation temperature close to that of the CMB. For molecules such as HF and HCl in which there are no metastable rotational states, this means that most molecules are found in the ground rotational state. For triatomic hydrides such as H_2O, H_2O^+, and H_2Cl^+ in which there are two spin symmetries (ortho with total H nuclear spin 1, and para with total H nuclear spin 0), most molecules in diffuse clouds are found in *one or other* of the lowest rotational states of the two spin symmetries. For symmetric top molecules such as NH_3 and H_3O^+, in which the rotation is characterized by the quantum numbers J and K, the lowest energy state for any given K is metastable. Thus for NH_3 and H_3O^+ in diffuse clouds, the population is largely divided amongst those metastable states lying at the bottom of each K-ladder.

While the CMB radiation is ubiquitous, other radiation fields can become important in specific environments: strong mid-IR and FIR radiation is present close to massive protostars, for example, and strong optical and UV radiation is present close to hot stars. Such radiation may affect the rotational populations in the ground vibrational state, as a result of pumping through rotational (FIR), vibrational (mid-IR) and electronic (optical and UV) transitions (Godard & Cernicharo 2013).

In different astrophysical environments, inelastic collisions with H_2, with H and/or with electrons can be important or even dominant in determining the equilibrium populations in the various rovibrational states of an interstellar hydride. Collisions with He can also be important but probably never play a dominant role. In dense, well-shielded molecular clouds, H_2 is the most important collision partner, but in photodissociation regions where the carbon is significantly photoionized, excitation by electrons

can be important or dominant. While the electron abundance in such regions is only $\sim$ few $\times 10^{-4}$ relative to H_2, the rate coefficients for electron impact excitation can exceed those for excitation by H_2 or H by four orders of magnitude, particularly in the case of hydride cations or neutral hydrides with large dipole moments: here, the cross-sections are enhanced by long-range Coulomb interactions (and the mean electron velocities exceed the mean H_2 velocities by the square root of the H_2 to electron mass ratio). In certain environments, and in particular the molecule reformation region behind dissociative shock fronts (see Section 5 below), excitation by atomic hydrogen can also be very important.

There is a considerable and ongoing effort to calculate state-to-state rate coefficients for various hydrides of astrophysical interest, most importantly in recent years for the excitation of water by ortho- and para-H_2 (Daniel, Dubernet & Grosjean 2011, and references therein) and by atomic hydrogen (Daniel et al. 2015). State-of-the-art quantal calculations make use of the so-called close-coupling method and rely upon accurate determinations of the potential energy surface for the system. Such calculations are computationally-expensive, and are often (e.g. in the case of water) limited to a subset of the rovibrational states that have actually been observed in interstellar hydrides. As a result, less computationally-intensive (and less accurate) methods such as quasi-classical trajectory calculations (e.g. Faure et al. 2007) must sometimes be used to interpret astronomical observations, in some cases accompanied by extrapolation methods involving propensity rules (e.g. Faure et al. 2007) or the use of artificial neural networks (Neufeld 2010). The LAMDA (Schöier et al. 2005) and BASECOL (Dubernet et al. 2013) databases have been established to collate collisional rate coefficients and spontaneous radiative decay rates for hydrides and other interstellar molecules in a standard format for use in modeling the excitation.

Formation pumping is a further process that can affect the excitation state of interstellar hydrides. Here, if the lifetime of the molecule is comparable to – or smaller than – the timescale on which the quasi-equilibrium level populations are established, the observed populations may reflect the initial conditions at formation. The most clearly-established case of formation pumping in interstellar hydrides is the excitation of high-lying OH rotational states following the photodissociation of H_2O to form OH (Tappe et al. 2008, discussed further in Section 5 below). Formation pumping has also been discussed as an explanation for the observed excitation of H_3O^+ (e.g. Lis et al. 2014; González-Alfonso et al. 2013), and may be important for other molecular ions as described further in Section 4 below.

2. CHEMISTRY

2.1. Gas phase processes

As anticipated in Section 1.2, hydrides are mostly formed in the gas through series of hydrogen abstraction reactions combined with dissociative recombination. The chemistry of carbon, oxygen and nitrogen hydrides is illustrated in **Figure 3**. This relative simplicity hides subtleties introduced by *i)* the presence of highly endothermic reactions on important pathways (e.g. the initiation reaction of the carbon chemistry between ionized carbon and molecular hydrogen has an endothermicity of 0.37 eV or 4300 K), and *ii)* the dependence of the reaction rates and products on the molecular hydrogen spin symmetry state, or more generally on the initial rovibrational state (for molecules) or the fine structure level (for atoms) of the reactants (e.g. Faure et al. 2013; Li et al. 2013). Fortunately, many of the key reactions for hydride synthesis have been studied through theoretical calculations and laboratory measurements because of their fundamental interest for molecular physics. For example, the neutral-neutral reaction between F and H_2 forming HF and H is one of the benchmark systems for the tunneling effect. Combining measurements down to 11 K and new theoretical calculations, Tizniti et al. (2014) have provided an accurate determination of this important reaction rate.

The hydrogen abstraction reactions initiating the oxygen, nitrogen, chlorine and argon chemistry

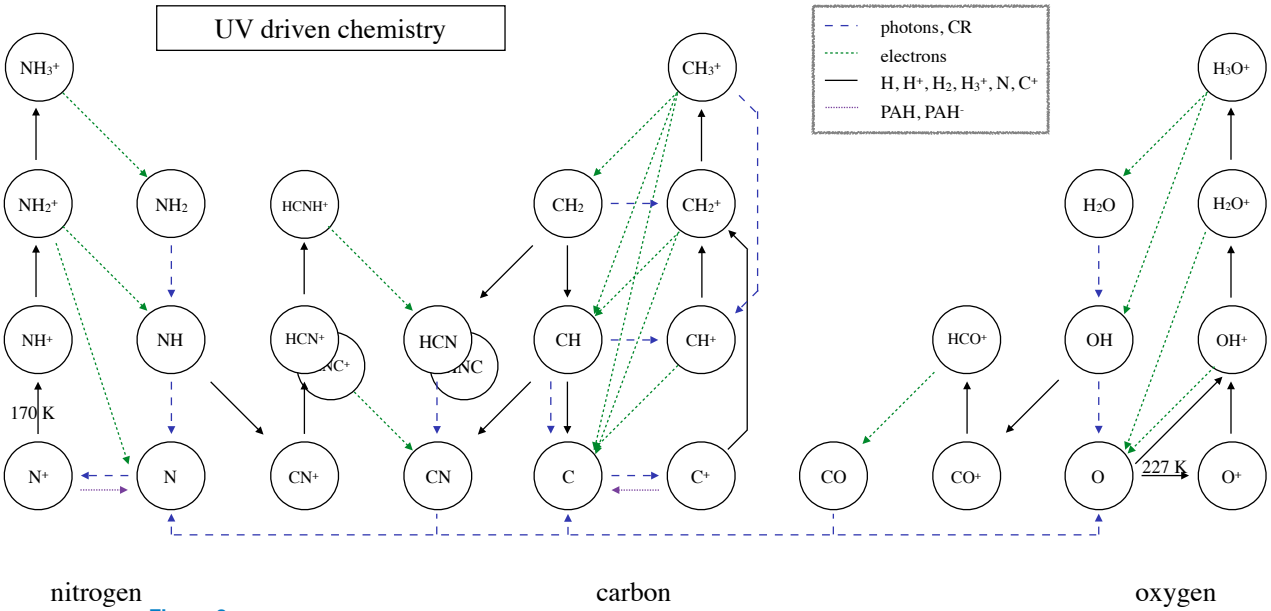

Figure 3

Illustration of the chemical network initiating the carbon, oxygen and nitrogen chemistry in diffuse cloud conditions (n_H = 50 cm^3, A_V = 0.4 mag, χ = 1). The black arrows show the reactions with H, H^+, H_2, H_3^+, C^+ and N, with values of the endothermicity for the reaction between N^+ and H_2 and for the charge exchange reaction between O and H^+. Note that CH_2^+ is formed in the slow radiative association reaction between C^+ and H_2. The dashed blue arrows indicate the reactions induced by far ultra violet (FUV) photons or cosmic rays. Dissociative recombination reactions with electrons are shown with green dotted arrows. Purple arrows show the neutralization reactions on dust grains and PAHs. Adapted from Godard, Falgarone & Pineau des Forêts (2014).

are exothermic or moderately endothermic (for N). Because dissociative recombination reactions are fast, photodissociation is usually not a dominant destruction process for the hydride ions, while it affects neutral hydrides. The hydride chemistry is sensitive to the strength and spectrum of the incident X-ray and UV radiation field, and to the ionization rate due to cosmic rays, the two main sources of ionized species. The exact energy distribution of the UV field is particularly important for the chlorine chemistry since the ionization potential of atomic chlorine, 12.968 eV, is very close to the Lyman edge (13.6 eV). Polycyclic Aromatic Hydrocarbons (PAHs) play a role in the chemistry because cations (e.g. H^+, C^+, N^+) get neutralized when encountering a neutral or negatively charged PAH. Hence PAHs reduce the efficiency of molecule formation. This is especially important for the oxygen chemistry in which the initiating charge exchange reaction between H^+ and O competes with neutralization on PAHs.

Given the relatively large reaction rates, the chemical time scales for gas phase hydride production are short, typically less than a few 100 yr provided molecular hydrogen has reached its equilibrium abundance. The formation of molecular hydrogen itself, which occurs on grain surfaces, is significantly slower, with typical time scales of 10 Myr for diffuse gas densities. Numerical simulations of the diffuse ISM, using either hydrodynamical or magnetohydrodynamic (MHD) codes, have shown however that the equilibrium molecular hydrogen fraction can be reached faster in a dynamical medium because the compressions induce transient density enhancements where H_2 forms more rapidly than in an uniform medium (Glover & Mac Low 2007). The time scale for conversion between the H_2 spin symmetry states strongly depends whether only gas phase processes contribute, or whether H_2 is

Cosmic Rays (CR): Cosmic Rays are energetic particles (electrons, protons, and heavier nuclei), accelerated at energies between 0.1 and 10^6 GeV in fast shocks.

PAHs: Polycyclic Aromatic Hydrocarbons are carbon and hydrogen molecules composed of multiple benzenic cycles with hydrogen atoms at the boundaries.

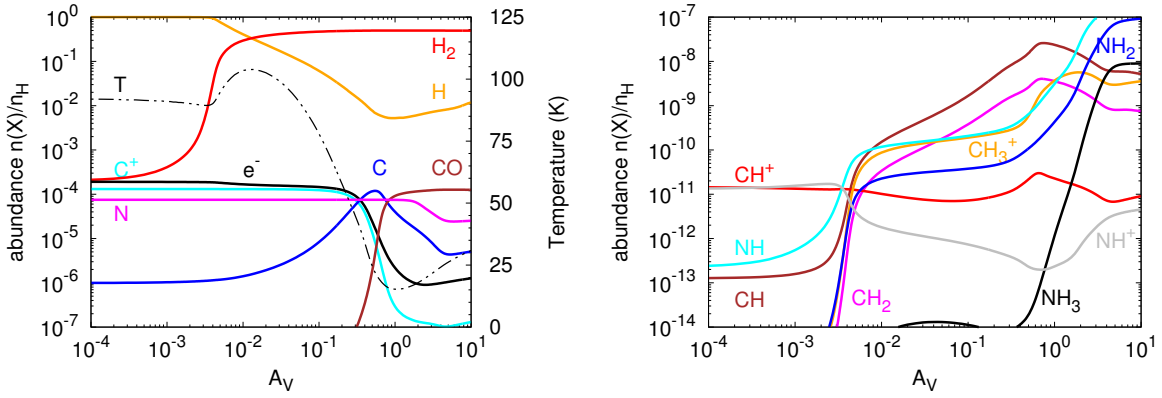

Figure 4

Variation of the gas phase abundances of various species relative to the total hydrogen content as a function of depth A_V for a cloud with constant pressure $P/k_B = 4 \times 10^3$ K cm^{-3}, irradiated by the average interstellar radiation field ($\chi = 1$) from the left side, and a cosmic ray ionization rate $\zeta_H = 2 \times 10^{-16}$ s^{-1}, computed with the Meudon PDR code (Le Bourlot et al. 2012). The left panel displays the hydrogen (H, H_2), carbon (C^+, C, CO), nitrogen (N, N_2 not shown) reservoirs together with the electron abundance and the kinetic temperature (right vertical scale). The gas density ranges from about 40 cm^{-3} at $A_V \sim 0.01$ mag up to $\sim$ 150 cm^{-3} at $A_V > 1$ mag. The right panel shows the main carbon and nitrogen hydride abundances as a function of extinction.

OPR: Ortho-to-para ratio, the ratio between the densities, or column densities, of the ortho and para nuclear spin symmetry states.

rapidly thermalized on dust grains (Le Bourlot 2000). In the former case, the conversion is slow, with a similar time scale as the static formation rate of H_2 (e.g. Pagani, Roueff & Lesaffre 2011). Conversion on grain surfaces is however expected to be faster, but a small fraction of o-H_2 ($\sim 10^{-3}$) is expected to remain even at low temperatures because of the presence of newly formed H_2 molecules, either on grains or through chemical reactions (Le Bourlot 2000). Several hydrides (e.g. NH_3, NH_2 or H_2O) exhibit spin symmetry states whose relative abundances are sensitive to the H_2 ortho-to-para ratio (OPR) in the gas.

State of the art chemical models predict with a good accuracy (better than a factor of two) the observed abundances of most of the abundant hydrides, and their respective relationships. **Figure 4** illustrates the behavior of carbon and nitrogen hydrides for a constant pressure cloud with $P/k_B = 4 \times 10^3$ K cm^{-3} using a pure gas-phase chemical network (except for H_2). The behavior of oxygen hydrides is illustrated in the left panel of **Fig.** 8 (Section 4) which displays a model with a similar value of the control parameter χ/n_H, where χ represents the enhancement factor of the incident FUV radiation field over the mean interstellar radiation field in the solar neighborhood. It is interesting to note that CH and CH_2 show a very similar behavior with a first rise of their relative abundances nearly coinciding with the H/H_2 transition at $A_V \sim 0.1$ for this particular model. The appearance of nitrogen hydrides (NH, NH_2 and NH_3) takes place further inside the cloud at $A_V \sim 1$, and coincides with the CO formation zone. The NH^+ abundance remains low, in agreement with *Herschel* observations (Persson et al. 2012). The series of molecular ions OH^+, H_2O^+ and H_3O^+ behaves somewhat differently from the carbon and nitrogen hydrides : each ion is predicted to probe a different zone of molecular hydrogen content, with $f_{H_2} = 2n(H_2)/[2n(H_2) + n(H)]$, the molecular fraction, increasing from OH^+ to H_3O^+. As will be discussed further in Section 7 below, this property is fully consistent with observations and can be used to derive the fraction of molecular hydrogen in the region of maximum OH^+ abundance.

2.2. Solid phase processes

Molecular hydrogen is not the only molecule formed in the solid phase. Recent studies have shown, that even under diffuse ISM conditions, the formation of molecules on grain surfaces can be efficient (see e.g. Sonnentrucker et al. 2015, for H_2O) . Hydrides are particularly susceptible to being formed on grain surfaces because of the ubiquitous presence of hydrogen. Laboratory experiments using beams of hydrogen and oxygen atoms hitting a cold surface have clearly demonstrated that water ice forms in this process. A fraction of the newly formed molecules does not stay on the cold surface but is immediately released in the gas phase (Dulieu et al. 2013), a process called chemical desorption. The fractions of trapped versus ejected molecules depend on the nature of the surface, the ice coverage, and the exact reaction mechanism. In a similar manner as water ice, the hydrogenation of carbon and nitrogen atoms produces methane and ammonia. Laboratory experiments are now able to probe these processes including exchanges between H and D atoms and the production of deuterated species (Fedoseev, Ioppolo & Linnartz 2015).

Once formed on the cold grain surfaces, four mechanisms may release molecules to the gas phase: *i)* thermal sublimation when the grains reach temperatures larger than the ice sublimation threshold, *ii)* photo-desorption when FUV photons are absorbed by the grain surface and kick some molecules out of the ice, *iii)* cosmic ray induced desorption when an energetic particle interacts with a grain mantle, and *iv)* chemical desorption during the formation process. Laboratory experiments have been performed to study these mechanisms and understand in which conditions they operate. Theoretical and laboratory studies of ice photodesorption have concluded that this process is complex. FUV photons can dissociate a frozen water molecule producing two fragments (H and OH) that have excess energy. These fragments can either recombine as a gas phase water molecule, or the excited H can kick out another frozen water molecule. The outcome depends on many parameters, first of all where the FUV photon is absorbed, since only the upper ice layers participate to the desorption. The presence of other isotopologues, of other molecules like CO, which does not dissociate upon the absorption of a FUV photon, will also affect the desorption yield. Overall the photodesorption yields range between 10^{-4} and 10^{-2} molecules/photon (Arasa et al. 2015). With such numbers, most of the species are predicted to be frozen in dense core conditions, with a minor fraction remaining in the gas phase. As illustrated in Fig. 8, water vapor reaches its peak abundance for extinctions of a few magnitudes. Chemical models also include a temporal dimension because the dynamical time scales, which scale with the free fall time $t_{ff} = \sqrt{3\pi/32G\rho} \sim 10^5 \sqrt{5 \times 10^4 \mathrm{cm}^{-3}/n(\mathrm{H_2})}$ yr, are similar to the chemical time scales. For instance, the freeze-out time scale in the absence of desorption is $t_{freeze} \sim 10^5 \left(10^4 \mathrm{cm}^{-3}/\mathrm{n(H_2)}\right)$ yr.

While the respective abundances of H_2O, CH_4 and NH_3 are fairly well documented in interstellar ices, little is known about the presence of hydrides composed of the heavier elements F, S or Cl in ices. The somewhat lower elemental abundances precludes a direct identification given the limited sensitivity of infrared spectroscopy of solid features, 1% of the water ice content. Solid phase and gas phase processes are coupled, as shown for instance by the production of H_2 and methane during the FUV irradiation of hydrogenated amorphous carbons (Alata et al. 2014). Although laboratory experiments have led to steady progress in the understanding of the solid phase chemistry, the state of the art is still far from that of the chemistry in gas phase, even for simple hydrides. The relative contributions of solid phase and gas phase routes to the formation of nitrogen hydrides deserves specific attention. While the reaction between N^+ and H_2 initiates the nitrogen chemistry in UV-illuminated regions, NH is mostly formed as as a minor channel in the dissociative recombination of N_2H^+ in shielded regions. As discussed by Wagenblast et al. (1993), the gas-phase production route for nitrogen hydrides is not efficient enough to explain the observed abundance in diffuse clouds, especially if the cosmic ray ionization rate is low. An alternative formation mechanism for nitrogen hydrides involves the hydrogenation of nitrogen atoms on grain surfaces to form ammonia, and its release into the gas phase for

further processing. Given the wealth of data now available, the relative contributions of solid phase and gas phase routes in the nitrogen chemistry should be assessed, especially for diffuse conditions. More generally, more quantitative evaluations of the reactivity of atoms and molecules (including diffusion) and of the efficiency of the various desorption processes is needed to improve astrophysical models.

3. HYDRIDES IN DIFFUSE GAS

3.1. Overview

With the exception of CH_4, CH_3^+ and NH_4^+, all the hydride molecules listed in Table 1 are known to be present in diffuse molecular clouds. Observations of hydrides in diffuse clouds have targeted transitions over a wide range of wavelengths, from a 122 nm electronic transition (of OH) to a set of 18 cm lambda-doubling transitions (also of OH). Typically, molecules in diffuse clouds have been observed in absorption toward background sources of continuum radiation; these include hot stars (at ultraviolet wavelengths), warm dust in regions of active star formation (at FIR and submillimeter wavelengths), and HII regions (at centimeter wavelengths). With the exception of those targeting centimeter-wavelength lambda-doubling transitions, absorption-line observations yield relatively robust and model-independent estimates of molecular column densities. This advantage results from the fact – discussed previously in Section 1.3 – that under typical conditions in diffuse clouds, most hydride molecules are found primarily in the ground state (or, for triatomic hydrides, in the lowest energy states of the ortho- and para-symmetry states); thus, stimulated emission is typically negligible, and the scaling between absorption line optical depth and molecular column density is only weakly dependent upon the physical conditions. In the remainder of this section, the observational data on hydride molecules in diffuse clouds will be reviewed. In Section 7 below, we will discuss how the measured abundances of interstellar hydrides can be used as quantitative probes of the environment in which they are found.

3.2. Optical/UV and centimeter-wavelength observations of interstellar hydrides

In diffuse molecular clouds, several hydride molecules show observable absorption at optical and ultraviolet wavelengths through their electronic transitions. These include three molecules – CH, CH^+, and NH – that were first detected (see Table 1) in this spectral region; two molecules – OH^+ (Krełowski, Beletsky & Galazutdinov 2010) and SH (Zhao et al. 2015) – with optical/UV transitions that were detected shortly after their initial discovery at submillimeter wavelengths; as well as OH, detected both at vacuum UV (e.g. Snow 1976) and near-UV wavelengths (e.g. Porras et al. 2014). In this spectral region, spectral resolving powers $R = \lambda/\Delta\lambda$ in excess of $\sim 10^5$ can be achieved with echelle spectrometers. Although not as high as those achievable at submillimeter wavelengths using heterodyne receivers, these spectral resolving powers yield valuable kinematic information about the absorbing molecules. For example, a recent analysis of near-UV spectra showing OH^+, OH, CH, CH^+, and CN absorption (Porras et al. 2014) has revealed a kinematic association between OH^+, CH^+, and neutral atoms on the one hand; and CN and OH on the other hand. CH is associated with both families, but with the largest CH column densities usually occurring in gas with a high molecular fraction. Because of the effects of dust extinction, optical/UV observations of absorption by molecules in the Galactic disk are limited to relatively nearby material, in contrast to the case of the submillimeter observations described in Section 3.3 below. At centimeter-wavelengths, two hydride molecules – OH (e.g. Allen, Hogg & Engelke 2015, and references therein) and CH (e.g. Chastain, Cotten & Magnani 2010) – have been widely observed in diffuse interstellar gas clouds, by means of their lambda-doubling transitions at 18 cm and 9 cm respectively. Such transitions, which are typically observed in emission,

Table 2 Typical hydride abundances in diffuse clouds

Molecule	Average abundance relative to H or H_2	Average abundance (fraction of gas phase elemental[a])	Method	Reference for hydride column densities
CH	3.5×10^{-8}	1.3×10^{-4}	V[b], UV[c], M[d]	Sheffer et al. (2008)
CH_2	1.6×10^{-8}	6×10^{-5}	S, CH, M	Polehampton et al. (2005)
CH^+	6×10^{-9}	4×10^{-5}	V, Re, M	Gredel (1997); Crane, Lambert & Sheffer (1995)
CH_3^+	$< 2 \times 10^{-9}$	$< 1.4 \times 10^{-5}$	Re, V	Indriolo et al. (2010)
NH	8×10^{-9}	6×10^{-5}	S, CH, 1	Persson et al. (2010)
NH_2	4×10^{-9}	3×10^{-5}	S, CH, 1	Persson et al. (2010)
NH_3	4×10^{-9}	3×10^{-5}	S, CH, 1	Persson et al. (2010)
NH^+	$< 4 \times 10^{-10}$	$< 6 \times 10^{-6}$	S, HI, 1	Persson et al. (2010)
OH	1×10^{-7}	1.6×10^{-4}	V, S, CH, M	Wiesemeyer et al. (2015); Lucas & Liszt (1996)
H_2O	2.4×10^{-8}	4×10^{-5}	S, CH, M	Flagey et al. (2013)
OH^+	1.2×10^{-8}	4×10^{-5}	S, HI, M[d]	Indriolo et al. (2015)
H_2O^+	2×10^{-9}	6.5×10^{-6}	S, HI, M[d]	Indriolo et al. (2015)
H_3O^+	2.5×10^{-9}	4×10^{-6}	S, CH, 1	Lis et al. (2014)
HF	1.4×10^{-8}	0.4	S, CH, M	Sonnentrucker et al. (2010)
SH	1.1×10^{-8}	4×10^{-4}	S, CH, M	Neufeld et al. (2015b)
H_2S	5×10^{-9}	1.8×10^{-4}	S, CH, M	Neufeld et al. (2015b)
SH^+	1.1×10^{-8}	8×10^{-4}	S, HI, M	Godard et al. (2012)
HCl	1.5×10^{-9}	0.004	S, CH, 1	Monje et al. (2013)
HCl^+	8×10^{-9}	0.04	S, CH, M	De Luca et al. (2012)
H_2Cl^+	3×10^{-9}	0.02	S, CH, M	Neufeld et al. (2015a)
ArH^+	3×10^{-10}	1×10^{-4}	S, HI, M[e]	Schilke et al. (2014)

[a]Assumes the following gas-phase elemental abundances relative to hydrogen in the diffuse ISM: carbon = 1.4×10^{-4}; oxygen = 3.1×10^{-4}; nitrogen = 6.8×10^{-5}; fluorine = 1.8×10^{-8}; sulphur = 1.4×10^{-5}; chlorine = 1.8×10^{-7}; argon = 3.2×10^{-6}

[b]Method for determination of hydride column density: V = visible or infrared observations of nearby stars; S = submillimeter, FIR (CH_2) or millimeter (H_2S) wavelength observations. Abundances determined from visible observations refer to the solar neighborhood while abundances determined from (sub)millimeter and FIR observations also probe the Galactic plane halfway between the Galactic center and the solar circle

[c]Method for determination of H_2 or atomic hydrogen column density: UV = UV observations of H_2 Lyman and Werner bands; Re = reddening of background star; CH = submillimeter observations of CH, for an assumed $N(CH)/N(H_2)$ ratio of 3.5×10^{-8}; HI = H 21 cm absorption line observations

[d]Sample size: M = average (median) over multiple sources; 1 = average (mean) over line-of-sight to W31C

[e]Median value excludes clouds in the Galactic Center, where the abundances are typically an order-of-magnitude higher

have provided a valuable tracer of molecular hydrogen, as discussed in Section 7 below.

3.3. FIR and submillimeter observations of absorption by interstellar hydrides

Over the past five years, *Herschel* and SOFIA have provided unique opportunities to observe submillimeter absorption by many interstellar hydrides in diffuse clouds along the sight-lines to bright submillimeter continuum sources. Heterodyne spectrometers available on both these observatories – the HIFI instrument on *Herschel* and the GREAT instrument on SOFIA – have provided extremely high (sub-km/s) spectral resolution that is unmatched by other spectrometric techniques operating at submillimeter, infrared or visible wavelengths. *Herschel* observations have led to the discovery of interstellar SH^+, HCl^+, H_2Cl^+, H_2O^+ and ArH^+, and the first extensive observations of HF and

Herschel: The *Herschel* Space Observatory, a FIR and submillimeter satellite observatory (55 - 672μm) with a 3.5 m primary mirror, operated by ESA between 2009 and 2013, and with important participation from NASA.

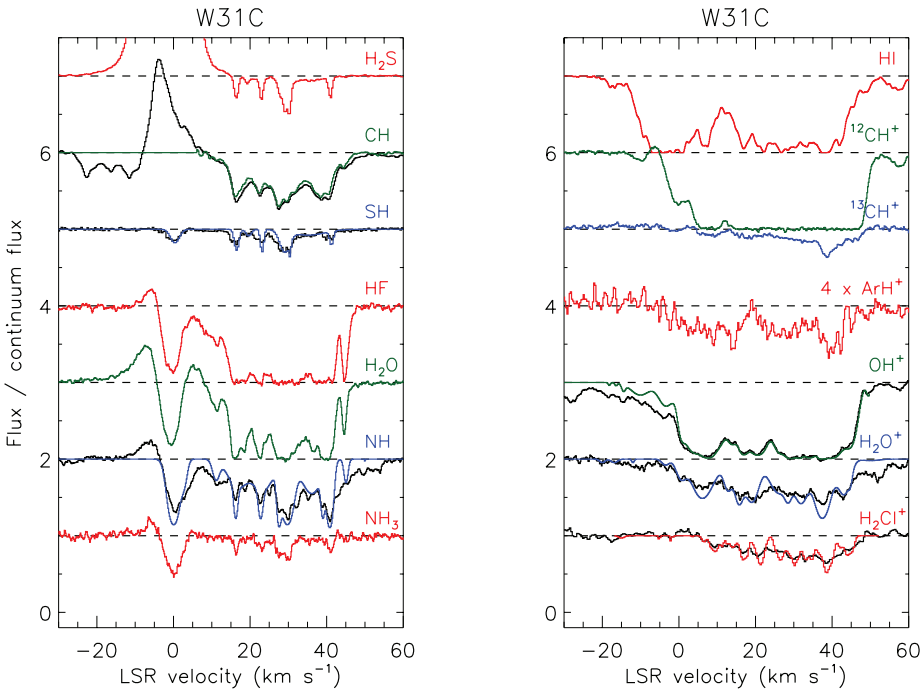

Figure 5

Absorption spectra observed toward W31C. Left panel from top to bottom: spectra of H_2S $1_{10} - 1_{01}$ at 168.8 GHz (based on data published by Neufeld et al. (2015a)); CH $^2\Pi_{3/2}$ $J = 3/2 - ^2\Pi_{1/2}$ $J = 1/2$ at 532.7/536.8 GHz (Gerin et al. 2010a); SH $^2\Pi_{3/2} J = 5/2 - 3/2$ at 1381 GHz Neufeld et al. (2015a); HF $J = 1 - 0$ at 1232 GHz; H_2O $1_{11} - 0_{00}$ at 1113 GHz (Neufeld et al. 2010); NH $J_N = 2_1 - 1_0$ at 974.5 GHz; NH_3 $J_K = 2_1 - 1_1$ at 1215.2 GHz (Persson et al. 2010). Right panel from top to bottom: HI 21 cm (Winkel et al. in preparation); $^{12}CH^+$ $J = 1 - 0$ at 835.1 GHz; $^{13}CH^+$ $J = 1 - 0$ at 830.2 GHz (Godard et al. 2012); ArH^+ $J = 1 - 0$ at 617.5 GHz (Schilke et al. 2014); OH^+ $^2\Pi_{3/2} J = 5/2 - 3/2$ at 971.8 GHz; H_2O^+ $1_{11} - 0_{00}$ at 1115 GHz (Gerin et al. 2010b); H_2Cl^+ $1_{11} - 0_{00}$ at 485.4 GHz (Neufeld et al. 2012). For species with a partially-resolved hyperfine splitting (CH, SH, NH, OH^+, H_2O^+), black histograms show the observations and color histograms show the hyperfine-deconvolved spectra. For clarity, the spectra are separated by vertical offsets. The ArH^+ spectrum is expanded by a factor 4 (in addition to being translated) so that the relatively weak absorption is clearer.

SOFIA: The Stratospheric Observatory For Infrared Astronomy is an airborne 2.7 m telescope, covering the wavelength range 1 - 655 μm, operated by NASA and the German Aerospace Center (DLR).

OH^+; SOFIA observations have enabled the first detection of interstellar SH, and the first heterodyne observations of the 2.5 THz ground state rotational line of OH.

Submillimeter absorption-line studies with *Herschel* and SOFIA have typically made use of strong continuum sources in the Galactic plane, at distances up to $\sim$ 11 kpc from the Sun and with sightlines that can intersect multiple diffuse clouds in foreground spiral arms. Thanks to the differential rotation of the Galaxy, different diffuse clouds along a single sightline give rise to separate velocity components in the observed absorption spectra. *Herschel* observations have been performed towards $\sim$ 20 such continuum sources, revealing $\sim$ 100 distinct components in which molecular column densities can be determined.

Figure 5 shows the spectra of a dozen hydride molecules observed along the sightline to W31C, a region of high-mass star formation located 4.95 kpc from the Sun, along with the HI 21 cm absorption line. All the spectra shown in Figure 5 show clear evidence for absorption by foreground material in

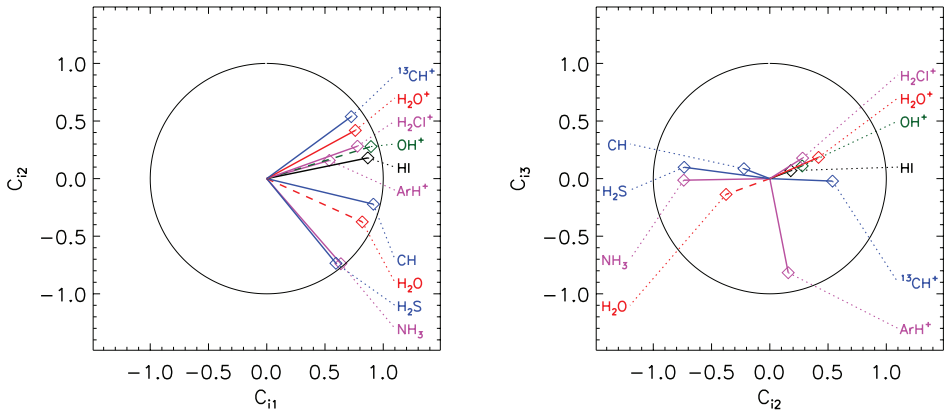

Figure 6

Results of PCA analysis for various species observed toward W31C, modified from Neufeld et al. (2015b).

diffuse clouds along the sight-line. For some molecules (e.g. SH and H_2S), the observed absorption is concentrated into five or six narrow features with linewidths $\sim 1 - 3\,\mathrm{km\,s^{-1}}$; other molecules – including most of the molecular ions – show a more extended distribution in velocity space and are less strongly concentrated into narrow absorption components. Neufeld et al. (2015b) have presented a more quantitative examination of the similarities and differences between these absorption spectra with the use of Principal Component Analysis (PCA). Here, each optical depth spectrum (i.e. plot of optical depth against velocity) is represented as a linear combination of a set of orthogonal (i.e. uncorrelated) eigenfunctions, S_j, the latter chosen such that the first eigenfunction contains as much of the variation as possible, the second eigenfunction containing as much of the remaining variation as possible, and so forth. Typically, the spectrum of any species, i, may be represented by a linear combination of the first two or three eigenfunctions, $C_{i1}S_1 + C_{i2}S_2\,(+C_{i3}S_3)$, which provides an excellent fit to the observed optical depth spectra, and the *coefficients* within that linear combination – C_{i1}, C_{i2}, and C_{i3} – can be used to describe the distribution of each absorbing species. **Figure 6** shows the first three coefficients obtained from a joint analysis of ten species along the W31C sightlines. Here, diamonds indicate the coefficients obtained for each species in the C_{i1} - C_{i2} (left panel) and C_{i2} - C_{i3} (right) planes, and solid lines connect the origin to each diamond. In the limit where the *first two* principal components account for most of the variation in the spectra, the diamonds in the left panel lie on the unit circle, as explained by Neufeld et al. (2015b); moreover, the angle between the lines corresponding to any pair of species in that limit is equal to the arccosine of their correlation coefficient. The PCA results confirm that most of the molecular ions show a common distribution, which is similar to that of atomic hydrogen, while most neutral species - particularly NH_3 and H_2S - tend to follow a distribution that is uncorrelated with HI. The ArH^+ molecular ion appears largely uncorrelated both with the other molecular ions and with the neutral molecules.

In Table 2, we summarize the typical hydride abundances derived for the diffuse ISM. In the case of molecular ions (with the exception of H_3O^+), these are shown relative to atomic hydrogen, whereas for neutral molecules, they are shown relative to H_2. In both cases, the corresponding abundances are also given relative to the gas-phase abundance of the relevant heavy element. The values shown in Table 2 indicate that most hydride molecules in diffuse gas are only minor reservoirs of the heavy element they contain, with most heavy elements remaining overwhelmingly in atomic or singly-ionized form. The notable exception is HF, which, in diffuse regions with a large molecular hydrogen fraction,

can account for most of the gas-phase fluorine. Chlorine is another element with a fairly strong tendency toward hydride formation; in clouds with a modest H_2 fraction, H_2Cl^+ can account for several percent of the gas-phase chlorine abundance. These behaviors are thought to reflect the thermochemical considerations summarized in Figure 2; fluorine and chlorine are the only elements that can react exothermically with H_2 when in their dominant stage of ionization (i.e. F and Cl^+) in diffuse clouds.

4. HYDRIDES IN DENSE, STRONGLY UV-IRRADIATED GAS

While many aspects of diffuse molecular clouds can be understood in the framework of low A_V, low FUV field PDR models (for a review see Hollenbach & Tielens 1999), in this section we focus on the presence of hydrides in more strongly UV-irradiated (χ>10^3 times the average interstellar radiation field), and denser gas (n_H>10^4 cm^{-3}). These are conditions typical of the *surface* of dense molecular clouds illuminated by nearby massive stars, and also of the outer layers of irradiated protoplanetary disks (e.g. proplyds). Such "dense PDRs" are regulated by the presence of stellar FUV photons up to several magnitudes of extinction (high A_V). UV photons with energies higher than 13.6 eV ionize hydrogen atoms but they are absorbed in the adjacent H II regions. FUV photons, however, do dissociate molecules and ionize molecules and atoms with ionization potentials below 13.6 eV (C, S, Si, Na, Fe, etc.). Therefore, like diffuse clouds, dense PDRs are predominantly neutral, with maximum ionization fractions of $n_e/n_H \simeq 10^{-4}$, roughly the gas-phase carbon abundance. The chemistry of dense PDRs is driven by photo-reactions (Sternberg & Dalgarno 1995) and is also characterized by the warm temperatures attained by the gas ($T \simeq$100-1000 K) and by the presence of large fractions of (FUV-pumped) vibrationally excited molecular hydrogen, H_2^* (e.g. Black & van Dishoeck 1987).

Despite the large FUV radiation fields, H_2 molecules form on the surfaces of relatively warm dust grains ($T_{dust} \gtrsim 50$ K for $\chi \gtrsim 10^3$, e.g. Cazaux & Tielens 2004; Bron, Le Bourlot & Le Petit 2014, and references therein). As the H_2 abundance increases from the PDR edge to the cloud interior, reactions of H_2 with neutral and singly ionized atoms initiate the chemistry and lead to the formation of hydrides. Owing to the higher gas and electron densities compared to diffuse clouds, the excitation temperatures rise above the background temperature and rotational line *emission* is observed. Recent detections in dense PDRs include NH_3, CH^+, SH^+, OH^+, H_2O, OH, HF, CH and H_2Cl^+ (e.g. Batrla & Wilson 2003; Habart et al. 2010; Goicoechea et al. 2011; Nagy et al. 2013; van der Tak et al. 2012, 2013; Neufeld et al. 2012).

4.1. The role of vibrationally excited H_2 in the chemistry

The absorption of FUV photons in the Lyman ($B\,^1\Sigma_u - X\,^1\Sigma_g^+$) and Werner ($C\,^1\Pi_u - X\,^1\Sigma_g^+$) bands produces molecular hydrogen in excited electronic states. 10% of absorptions are followed by emission into the unbound continuum, leading to dissociation of the molecule. 90% of the absorptions, however, are followed by rapid radiative decay to the ground electronic state X. See an early historical review by Field, Somerville & Dressler (1966) and later quantitative developments by e.g. Black & Dalgarno (1976, and references therein). PDRs thus naturally produce large fractional abundances, f^*=$n(H_2\ v\geq1)/n(H_2\ v$=0), of vibrationally excited molecular hydrogen, H_2^*. In low density PDRs ($\lesssim 10^4$ cm^{-3}) H_2 is excited by FUV absorption followed by radiative fluorescent emission. The main gas heating mechanism is the photoelectric effect on PAHs and grain surfaces. For higher gas densities, collisional de-excitation through inelastic H-H_2 and H_2-H_2 collisions start to be important, and collisional de-excitation of FUV-pumped H_2 can dominate the gas heating. In addition, pure rotational lines of HD (Wright et al. 1999) and H_2 (Allers et al. 2005) can been detected. Their low critical densities make them good diagnostics of the warm gas temperature.

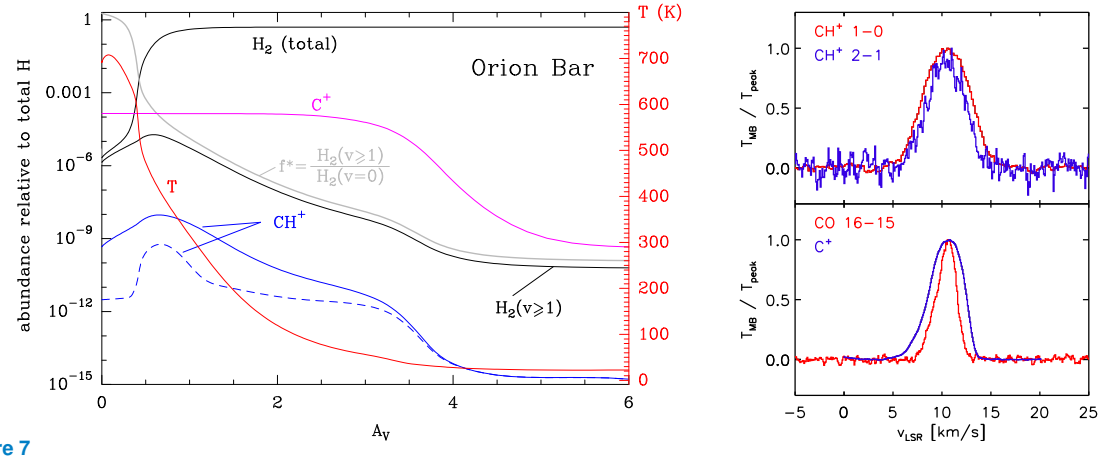

Figure 7

(Left): PDR model adapted to the physical conditions in the Orion Bar: n_H=10^5 cm^{-3} and χ=3×10^4. Abundances relative to n_H are shown for H_2, H_2(v≥1)=H_2^*, C^+, and CH^+ as a function of depth A_V into the cloud. Also shown is f^*=n(H_2 v≥1)/n(H_2 v=0), the fraction of vibrationally excited H_2 with respect to the ground vibrational state, and the gas temperature T. For the CH^+ abundance profile, the dashed line is for a specific model that only considers reactions of C^+ with H_2 in the ground vibrationally state (v=0). The continuous curve shows the CH^+ abundance including also state-to-state reactions of C^+ with H_2^* (adapted from Agúndez et al. 2010). (Right): Velocity-resolved observations of the Orion Bar with *Herschel*/HIFI. CH^+ J=1-0 and 2-1 lines are broader than those of [CII] and CO J=16-15. This may be the signature of formation pumping as explained at the end of Sect. 4.3 (from Nagy et al. 2013).

The H_2 v=1 levels have energies >0.5 eV (~5800 K) above the ground state v=0 and this energy can be used to overcome the endothermicity (or energy barrier) of chemical reactions involved in the formation of some hydrides, thus enhancing their production rate in PDRs. A very favorable case is CH^+. As previously noted, the $C^+ + H_2 \rightarrow CH^+ + H$ reaction is endothermic by ~4300 K (see Figure 2), temperatures (T>1,000 K) are required to produce significant amounts of CH^+ when H_2 is in the v=0 state. Laboratory experiments (Hierl, Morris & Viggiano 1997) and quantum calculations (e.g. Zanchet et al. 2013b), however, show that the reaction becomes exothermic when H_2^*, and not H_2(v=0), is the reactant. The reaction rate k^* then reaches the Langevin limiting case, and becomes almost independent of the temperature. In practice, enhanced XH^+ (or XH) hydride abundances will be produced through reactions $X^+ + H_2^* \rightarrow XH^+ + H$ (or $X + H_2^* \rightarrow XH + H$) if the product $f^* \Delta k\,(T)$ is larger than 1. Here, $\Delta k\,(T) = k^*\,(T)/k^0\,(T)$ is the reaction rate ratio when H_2^* and H_2(v=0) are the reactants respectively (see Agúndez et al. 2010). In addition, $k^*\,(T)$, the specific reaction rate with H_2^*, has to be large enough compared to other reactions removing the atom X^+ (or X), for example, X^+ neutralization reactions with PAHs and small grains.

Rotationally excited CH^+ emission lines were first detected toward planetary nebula NGC 7027 (Cernicharo et al. 1997). These lines arise from the warm and dense PDR surrounding the ionized nebula that is irradiated by the strong UV field from the hot central star ($T_{\rm eff}$≈200,000 K). The same pure rotation emission lines have been detected in the Orion Bar (Nagy et al. 2013, see **Figure 7 right**) and in the irradiated surface of the protoplanetary disk around Herbig Be star HD 100546 (Thi et al. 2011). As there is no reaction pathway that can efficiently produce CH^+ in FUV-shielded cold gas, CH^+ is expected to peak near the PDR edge where C^+ and H_2^* are abundant (see **Figure 7 left**). A similar argument applies to SH^+, with the difference that the $S^+ + H_2 \rightarrow SH^+ + H$ reaction is even more endothermic (~10,000 K) and only becomes exothermic when H_2^* is in the v=2 or higher vibrational states (Zanchet et al. 2013a). Line emission from both ions has been observed in the Orion Bar with

ALMA: The Atacama Large Millimeter/submillimeter Array is an ensemble of 66 (sub)millimeter telescopes operating between 80 and 900 GHz.

Herschel (Nagy et al. 2013), but $^{13}CH^+$ and SH^+ can be detected from ground-based telescopes such as ALMA. Note that rotationally excited CH^+ has also been recently observed in visible absorption (Oka et al. 2013) toward lower density PDR environments close to hot massive stars, where vibrationally excited H_2 is also observed in FUV absorption (Rachford, Snow & Ross 2014).

The role of FUV-pumped H_2^* in the chemistry may also be important at the scales of entire molecular cloud complexes. In template star-forming regions like Orion, >98% of the large-scale near-IR H_2 emission is thought to arise from FUV-excited fluorescent emission in PDR gas (Luhman et al. 1994). This widespread H_2^* emission traces the extended molecular gas that is illuminated by the strong FUV radiation field from massive stars in the Trapezium cluster. Its presence likely explains the large-scale CH^+ J=1-0 emission detected in Orion molecular cloud (J.R. Goicoechea priv.comm.). The high abundances of H_2^* in local massive star-forming regions may have consequences for the interpretation of hydride spectra in the extragalactic context, as many actively star-forming galaxies are dominated by PDR emission. In diffuse molecular gas (much lower density and FUV fluxes), the H_2^* abundance and f^* fractions are significantly lower. Indeed, the large CH^+ and SH^+ column densities inferred from line absorption observations of diffuse clouds cannot be explained by standard PDR models adapted to the $n_H \simeq 100\,cm^{-3}$ and $\chi \simeq 1$ conditions prevailing in these clouds (e.g. Godard et al. 2012, and references to older models therein).

4.2. Oxygen hydrides

Relatively low water vapor abundances are expected in dense PDRs. H_2O has a high adsorption energy and thus it freezes at T_{dust}<100 K in dense cloud conditions (as compared to ~20 K for CO). Photodesorption of water ice mantles takes place in PDRs but H_2O molecules are readily photodissociated by the intense FUV radiation field (Hollenbach et al. 2009). This process results predominantly in OH + H (e.g. van Dishoeck, Herbst & Neufeld 2013, hereafter vD13). Low excitation H_2O rotational lines have been observed toward high FUV flux PDRs such as the Orion Bar (Habart et al. 2010; Choi et al. 2014) and Mon R2 (Pilleri et al. 2012). The inferred gas-phase H_2O abundances are below a few 10^{-7}. Rotationally excited OH emission lines have been also detected in the Orion Bar. They are consistent with a OH/H_2O>1 column density ratio (Goicoechea et al. 2011), similar to the diffuse cloud values, whereas OH/H_2O<1 ratios are typically observed toward warm shocked gas (see next Section). Regarding OH formation, the dominant route near the edge of a strongly UV-irradiated PDR is the endothermic reaction $O + H_2 \rightarrow OH + H$ (see the first OH abundance peak in **Figure 8 right**). However, the reaction remains slow when the H_2 is vibrationally excited (Sultanov & Balakrishnan 2005). Consequently, the OH formation rate is likely more sensitive to the gas temperature than to the H_2^* abundance. For lower FUV fields and temperatures, OH forms from H_3O^+ electron recombination and from grain surface reactions (e.g. Hollenbach et al. 2009, 2012).

In the Milky Way, OH^+ rotational line *emission* has been detected toward high electron density environments: the Orion Bar (van der Tak et al. 2013), planetary nebulae hosting hot central stars with T_{eff}>100,000 K (Aleman et al. 2014), and toward the Supernova remnant in the Crab Nebula (Barlow et al. 2013). The non-detection of H_2O^+ and H_3O^+ emission in these environments indicates that OH^+ lines arise in gas layers where most hydrogen is in atomic form, and OH^+ is predominantly formed by the $O^+ + H_2 \rightarrow OH^+ + H$ exothermic reaction. Figure 8 left shows predictions of a steady-state PDR model for a $n_H = 10^4\,cm^{-3}$ cloud illuminated by a FUV field that is 100 times the mean ISRF. These conditions are representative of a molecular cloud close to massive O and B stars. The model includes reactions with PAHs and freeze-out of gas-phase species (important at A_V>4). It shows that OH^+ peaks closer to the PDR edge than other oxygen hydrides. Figure 8 right shows the results for a higher density, $n_H = 10^6\,cm^{-3}$, and higher FUV irradiation model, $\chi = 10^5$. These conditions are more typical of

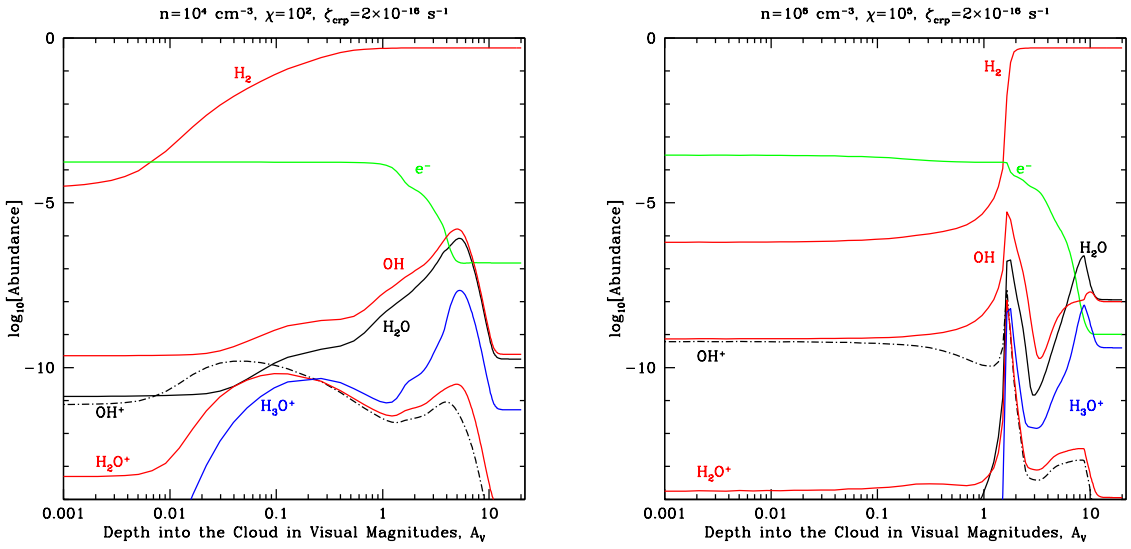

Figure 8

Predicted gas-phase abundances of several hydrides with respect to H nuclei as a function of depth A_V into the cloud for PDRs with n_H=10^4 cm^{-3}, χ=100, and ζ_{CR}=2×10^{-16} s^{-1} (left), and with n_H=10^6 cm^{-3} and χ=10^5 (right). From Hollenbach et al. (2012).

the compressed PDR layers at the boundary of a H II region surrounding a massive star or the surface layers of protoplanetary disks. In this model, H_2 collisional de-excitation dominates the gas heating and the gas attains higher temperatures ($T\simeq1000$ K at $A_V\simeq1$). This triggers a fast warm gas-phase in which many endothermic reactions can proceed rapidly. The dense PDRs located at the walls of outflow cavities irradiated by a high mass young stellar object have been modeled by Bruderer et al. (2010), who predicted high abundances of CH^+, OH^+ and NH^+ within such regions.

4.3. Formation pumping and the excitation of reactive hydride ions

Reactive collisions (collisions that lead to a chemical reaction) influence the excitation of molecules when the time-scale of the chemical reaction becomes comparable, or shorter, than that of nonreactive collisions. This makes the lifetime of the molecule so short that it does not get "thermalized" by collisions with non reactive species, or by radiative absorptions of the background radiation field. This is referred to as "formation pumping", the molecule retains an excited state due to its formation, and a proper treatment of the molecule excitation requires including chemical formation and destruction rates in the statistical equilibrium calculation determining the level populations (e.g. Black 1998). Reactive ions such as CH^+ or OH^+ are a special kind because they can be destroyed on nearly every collision with the most abundant species: H_2, H and e^- (OH^+ in particular does not react with H). Detailed CH^+ excitation models show that formation pumping dominates the population of CH^+ rotationally excited levels in PDRs such as the Orion Bar (Godard & Cernicharo 2013). In addition, the effects of molecule destruction and molecule formation in excited levels needs to be taken into account in chemical networks. It is becoming common to refer to "state-to-state" chemistry when the specific state-dependent reaction rates are included in models.

Reactions of C^+ with $H_2(v=0, J>7)$ or with $H_2(v\geq1)$ are exothermic and drive the CH^+ production in PDRs such as the Orion Bar (see Section 4.1). Therefore, CH^+ formation results in an excess of

energy equivalent to several thousand K. This energy may be redistributed into translational motion of the newly formed CH^+ molecules (Black 1998). CH^+ reacts so quickly with H, H_2 and electrons that its translational motions may never thermalize to the gas kinetic temperature. The broader CH^+ J=1-0 emission line widths observed toward the Orion Bar ($\sim$5.5 km s^{-1}, corresponding to a temperature of several thousand K) compared to those of other molecular lines (usually $\sim$2-3 km s^{-1}, see Figure 7 right) has been interpreted as the signature of CH^+ formation pumping and of non-thermal velocity distributions (Nagy et al. 2013). Formation pumping also influences OH^+ excitation (Gómez-Carrasco et al. 2014) and may also explain the broad OH^+ emission lines (van der Tak et al. 2013).

5. HYDRIDES IN SHOCKS AND TURBULENT DISSIPATION REGIONS

5.1. Shocks

Several astrophysical phenomena – including protostellar outflows and supernovae – give rise to supersonic motions in the interstellar medium, and these motions can drive shock waves that heat and compress the gas. Such shock waves modify both the chemistry of – and the emission from – interstellar hydrides, greatly enhancing the abundances of certain species, populating high-lying rotational states, and triggering strong maser amplification in specific transitions of OH and H_2O.

The chemical effects of shock waves include the sputtering of dust grains, which releases grain materials into the gas-phase, and the enhancement of gas-phase endothermic reactions that are negligibly slow at the typical temperatures ($T \leq 80$ K) of cold interstellar gas clouds but can become rapid behind shock waves. In dense molecular clouds, where dust grains are coated with icy grain mantles, the sputtering of grain mantles has a profound effect upon the water vapor abundances behind shocks. The sputtering process has been the subject of several theoretical studies (Draine, Roberge & Dalgarno 1983; Jiménez-Serra et al. 2008; Gusdorf et al. 2008), which suggest that grain mantles are completely removed in shocks propagating at velocities, v_s, larger than $\sim 20 - 25$ km s^{-1}, resulting in the release of water and other volatile grain mantle materials into the gas-phase. Observationally, the interstellar water vapor abundance measured by satellite observatories such as the *Submillimeter Wave Astronomy Satellite* (SWAS), Odin and *Herschel* is known to vary by more than three orders of magnitude (see vD13 and references therein), with the largest abundances observed in warm shocked regions associated with protostellar outflows and supernova remnants. Here, the water vapor abundance can reach several $\times 10^{-4}$ relative to hydrogen nuclei, an abundance comparable to that of carbon monoxide. However, many determinations of the water vapor abundances in shocked regions (vD13, their Table 4) are considerably smaller and lie below the predictions for shocks capable of sputtering icy grain mantles. This discrepancy may reflect the fact that many abundance determinations are averages over a mixture of shocks of varying velocity, some of which are too slow to sputter mantles, or due to UV irradiation of the shocked gas lowering the H_2O abundance and enhancing OH (Karska et al. 2014; Goicoechea et al. 2015). In a recent study (Neufeld et al. 2014) of the far-IR line emission detected by *Herschel* and *Spitzer* from shocked gas in NGC 2071, W28, and 3C391, the relative line intensities for multiple transitions of H_2O, CO and H_2 were found to be in acceptable agreement with standard theoretical models for nondissociative shocks that predict the complete vaporization of grain mantles in shocks of velocity $\sim$ 25 km s^{-1}, behind which the characteristic gas temperature is $\sim$ 1300 K and the H_2O/CO ratio is 1.2.

The second chemical effect of shock waves is to selectively increase the abundances of molecules that can be produced rapidly by endothermic reactions that are slow at the temperatures of cold quiescent gas clouds. Behind shock waves, elevated gas temperatures $\sim$ few $\times 10^2$ to $\sim$ few $\times 10^3$ K can be sufficient to overcome the barriers for several of the endothermic H-atom abstraction reactions listed in Fig. 2, greatly increasing the predicted abundances of CH^+, SH^+, CH, SH, OH and H_2O. In addi-

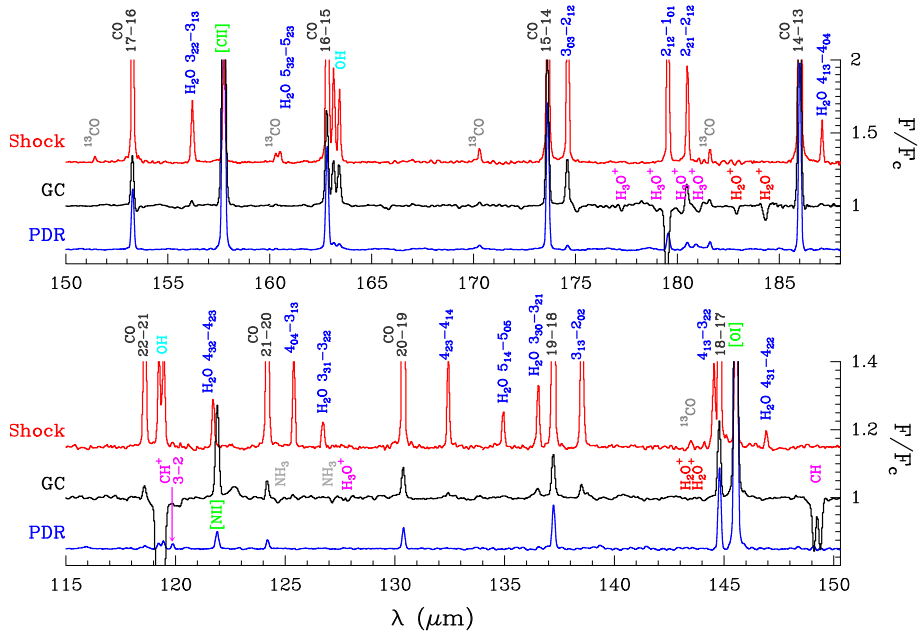

Figure 9

Comparative FIR spectra of three template environments in the Milky Way taken with *Herschel*/PACS between 115 and 188 μm: a molecular outflow and associated shocked gas, the Galactic Center, and a highly UV-irradiated PDR. They correspond, from top to bottom, to Orion BN/KL outflows (red, Goicoechea et al. 2015), the circumnuclear disk around Sgr A* (black, Goicoechea et al. 2013), and the Orion Bar PDR (blue, Joblin et al. in prep.). The ordinate scale refers to the line flux to continuum flux ratio, and the abscissa to the wavelength in microns. The "shock" and "PDR" spectra have been shifted from the F/F$_c$=1 level for clarity.

tion to the effects of the elevated temperatures behind interstellar shock waves, velocity drifts between the ions (which are coupled to the magnetic field) and the neutral species (which are not) can lead to an additional enhancement in the rates of ion-neutral reactions. Magnetohydrodynamic shock waves propagating at $\sim$ 10 km s^{-1}, in which such velocity drifts are present, have been invoked (e.g. Draine & Katz 1986; Pineau des Forêts, Roueff & Flower 1986; Pineau des Forêts et al. 1986) to explain large discrepancies between the observed abundances of CH^+, SH^+, and SH in diffuse molecular clouds and the predictions of standard photochemical models for cold ($T \leq 80$ K) diffuse gas.

In addition to their chemical effects, shock waves propagating in dense molecular gas also populate high-lying rotational states of hydrides that lead to a distinctive emission spectrum dominated by high-lying, collisional-pumped rotational transitions of H_2, CO, H_2O, and OH (Chernoff, McKee & Hollenbach 1982; Draine & McKee 1993). **Figure 9** shows a comparison of the FIR spectra of three environments : a molecular outflow and associated shocked gas, the Galactic Center combining dense gas and foreground absorption by diffuse gas, and a highly UV-irradiated dense PDR. While the shocked region shows intense OH and H_2O emission lines, the dense and warm environment of the Galactic Center region has a more diverse spectrum with other hydrides like NH_3, H_3O^+ and H_2O^+ showing up, indicating the presence of UV and CR irradiated molecular gas. The PDR spectrum is dominated by strong [CII] and [OI] emission, with faint lines from H_2O and rotationally excited CH^+.

In the case of OH, mid-IR transitions with upper state energies, E_u/k_B of several 10^4 K can also be excited following the photodissociation of H_2O by shock-generated UV radiation; this phenomenon,

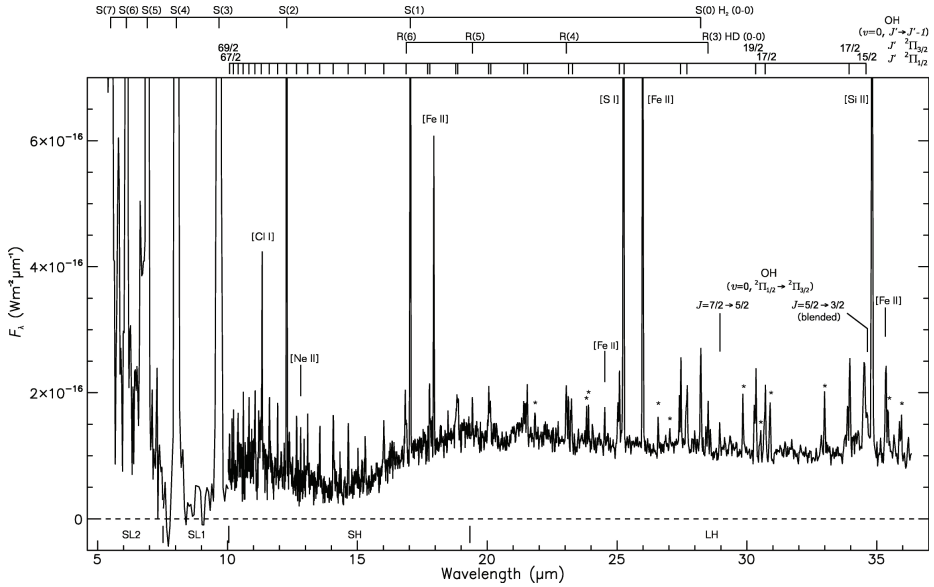

Figure 10

Spitzer spectrum obtained toward HH 211 (Tappe et al. 2008). Pure rotational lines of OH, with upper states with J up to 69/2, are clearly detected. Features marked with an asterisk are pure rotational transitions of H_2O.

observed by *Spitzer* toward HH 211 and illustrated in **Figure 10** (Tappe et al. 2008), occurs because the photodissociation of H_2O following absorption of Lyman alpha radiation leaves OH in states of rotational quantum number 30 - 50.

Along with the normal (non-inverted) OH and H_2O line radiation emitted by warm shocked regions, strong maser action is observed in several transitions : these include the 22 GHz $6_{16} - 5_{23}$ transition of H_2O, frequently observed from outflow-driven shock waves along with several submillimeter water maser transitions (e.g. Neufeld et al. 2013, and references therein), and the 1720 MHz transition of OH, a signpost of supernova-driven shock waves (e.g Frail & Mitchell 1998). Maser lines are typically characterized by small spots of emission, often unresolved even in long-baseline interferometric observations, narrow line width, and variability on timescales of months or less. Emission in the 22 GHz water maser transition, in particular, can achieve extraordinarily high brightness temperatures that may exceed 10^{14} K. Theoretical models for water maser emissions invoke either fast, dissociative jump ("J"-type) shocks (Elitzur, Hollenbach & McKee 1989; Hollenbach, Elitzur & McKee 2013), or slower non-dissociative "C-type" shocks in which the fluid velocities vary continuously (Kaufman & Neufeld 1996). Where multiple water maser transitions are observed, maser line ratios can provide constraints on the gas temperature in the masing region and the nature of the shocks that are present. Paradoxically, non-dissociative shocks can produce hotter *molecular* material than faster dissociative shocks, where molecules are quickly destroyed behind the shock front and are reformed only after the gas has cooled to $\sim$ 500 K. In some maser sources, gas temperatures of at least $\sim$ 900 K are implied by the observed water maser line ratios, indicating the presence of non-dissociative shocks (Melnick et al. 1993). Where supernova-driven shock waves encounter molecular clouds, widespread 1720 MHz OH maser emission is observed; here, the enhanced column densities of OH needed to explain the observed maser emission are believed to result from the effects of X-rays and/or cosmic rays in dissociating H_2O to form OH (Wardle & Yusef-Zadeh 2002).

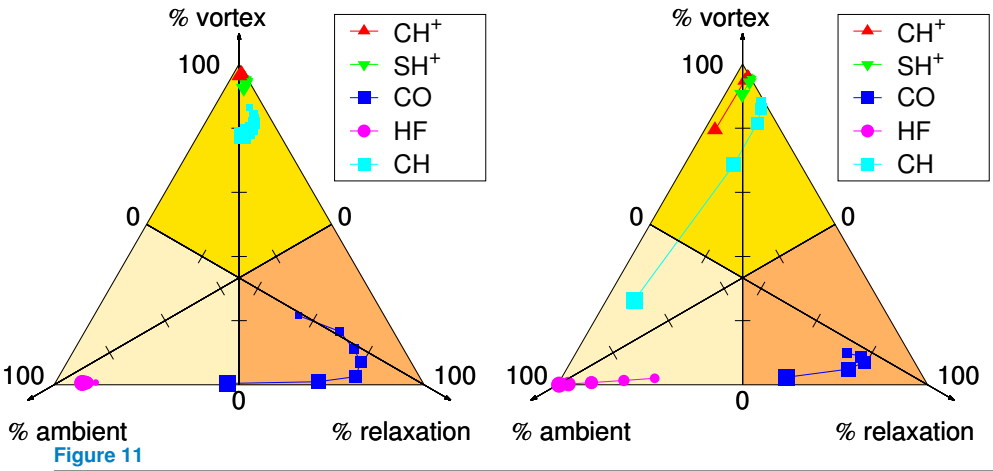

Figure 11

Ternary diagram for the TDR model of Godard, Falgarone & Pineau des Forêts (2014), indicating the fraction of each of five diatomic molecules found in three components (see text) of a diffuse cloud. The left panel displays model results for a gas density $n_{\rm H} = 50\,{\rm cm}^{-3}$, and for several values of the visual extinction, $A_{\rm V}$: 0.1, 0.2, 0.3, 0.4, 0.6, 0.8, and 1.0 mag in order of increasing symbol size. The right panel displays results for several values of the density, $n_{\rm H}$: 20, 30, 50, 100 and 300 cm^{-3}, at $A_{\rm V} = 0.4$ mag.

5.2. Turbulent dissipation regions

Turbulent dissipation regions (TDR; Godard, Falgarone & Pineau Des Forêts 2009; Godard et al. 2012; Godard, Falgarone & Pineau des Forêts 2014) represent an alternative but related scenario in which endothermic reaction rates can be enhanced as a result of locally-elevated gas temperatures and ion-neutral drift. In this scenario, molecules are produced in turbulent dissipation regions, represented as vortices in which the ion-neutral drift is induced by the ambient magnetic field. Model parameters include the physical conditions in the ambient medium (n, χ, A$_V$, ζ) along with four adjustable variables describing the turbulence dissipation rate, the ion-neutral drift, the vortex magnitude and lifetime. Given reasonable assumptions about the parameters that describe the turbulence, TDR models have been successful in accounting for the observed abundances of CH$^+$, SH$^+$ and SH in diffuse molecular clouds. **Figure 11**, a ternary diagram from the recent study of Godard, Falgarone & Pineau des Forêts (2014), shows – for five diatomic molecules – the relative fractions of the total column density in three separate components: (1) ambient material currently unaffected by turbulent dissipation; (2) material within the vortices that are the assumed sites of turbulent dissipation in this model ("vortex"); (3) material that has passed through a dissipative vortex and is currently relaxing to the ambient chemistry ("relaxation"). This model indicates that the, CH$^+$ and SH$^+$ column densities are dominated by material in dissipative vortices (component 2); the HF column density, by contrast, originates primarily in the ambient gas (component 1). The behavior of CH depends on the density, with the dominant component switching from vortex (component 2) to the ambient gas (component 1).The different behaviors predicted for these four hydrides reflect the fact that the production of CH, CH$^+$ and SH$^+$ is endothermic, while that of HF is exothermic. While the extensive chemical calculations leading to the results shown in Fig. 11 are based upon a simple characterization of interstellar turbulence with several adjustable parameters, a complementary approach makes use of more sophisticated numerical simulations of turbulence (Myers, McKee & Li 2015). To date, studies adopting the latter approach have included a more limited chemistry focused on the CH$^+$ problem.

TDR: Turbulent Dissipation Region

In both shocks and TDRs, the dynamical timescales can be short compared to the time needed to

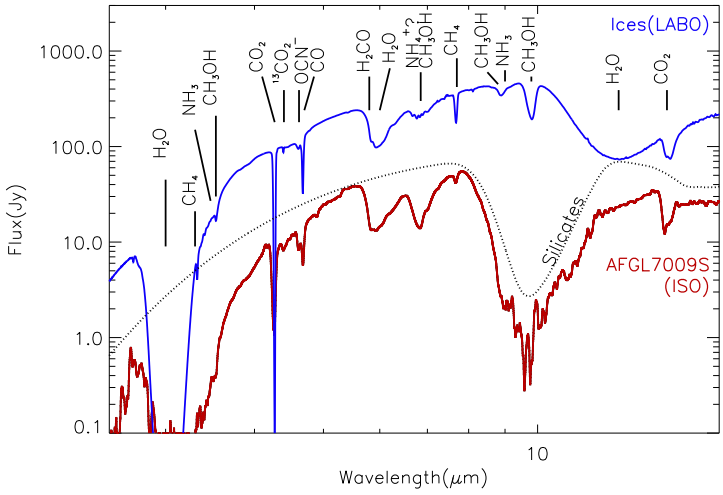

Figure 12

Comparison between the *ISO-SWS* spectrum toward the massive protostar RAFGL7009S (red line) and a laboratory transmission spectrum (blue line). The dotted lines shows the dust continuum including absorption from silicates. The positions of the main ice constituent absorption lines are indicated (adapted from Dartois et al. 1998).

establish a chemical equilibrium in which the rates of molecular formation and destruction are equal; a time-dependent treatment of the chemical rate equations is therefore needed. Simple shock models are sometimes described as "steady-state" models if the physical and chemical conditions are non-varying in a particular inertial frame, but the meaning here is different from "chemical quasi-equilibrium" in which the net rates of formation and destruction are nearly equal for each species. We note also in this context that even "chemical quasi-equilibrium", which is often a good approximation where shocks and TDRs are absent, is quite different from thermochemical equilibrium (TE), in which the rate of every chemical process equals that of its *reverse process* and the molecular abundances are determined solely by thermodynamics. The condition of TE *never* applies in the ISM, because of the presence of cosmic-rays and – in diffuse and translucent interstellar clouds – of UV radiation that would be entirely absent in thermal equilibrium at the gas kinetic temperature.

6. HYDRIDES IN DENSE AND SHIELDED GAS

Many neutral hydrides stay abundant in shielded regions, even in dense prestellar and protostellar cores. At the low gas and dust temperatures of these regions ($\sim$ 10 K), molecules freeze on dust grains, building an ice layer. Ice mantles also grow thanks to the condensation of atoms, which, by hydrogenation, contribute to the formation of saturated hydrides: H_2O for oxygen, CH_4 for carbon and NH_3 for nitrogen. **Figure 12** shows a representative IR spectrum of a massive star forming region with prominent absorption features tracing the composition of the ice mantle. Water ice is the dominant species, with NH_3 and CH_4 reaching a few percent of the water ice (Boogert, Gerakines & Whittet 2015).

The low temperatures ($T \sim 10$ K) and absence of FUV radiation represent a favorable environment

for fractionation, the chemical process leading to a higher fraction of an isotope in a given molecule (an isotopologue) than the ratio of the elemental abundances. The most efficient process is deuterium fractionation, in which one or several hydrogen atoms are substituted by deuterium atoms. As reviewed by Caselli & Ceccarelli (2012), deuterium fractionation can be very efficient in cold regions, with several molecules reaching abundance ratios [XH]/[XD] exceeding one percent, while the elemental D/H ratio is about 2×10^{-5}. Fractionation may also involve other isotopes like ^{13}C, ^{18}O, ^{17}O or ^{15}N. Fractionation in D or ^{15}N are studied to relate ISM processes with the formation of the first solids in the solar system, since primitive material shows localized D and ^{15}N enhancements (Aléon 2010).

In the dense gas around protostars ($n(H_2) > 10^7 cm^{-3}$), the dust temperature increases up to the ice sublimation threshold ($T \sim 100$ K for water ice). The gas phase abundances of neutral hydrides significantly increase in these hot cores (for massive stars) and hot corinos (for low mass stars). These objects exhibit a rich spectrum, including numerous hydride emission lines at (sub)millimeter wavelengths (e.g. Figure 9), and absorption lines in the infrared, revealing a high abundance of water vapor (Boonman et al. 2003), methane and CH_3 (*e.g.* Knez et al. 2009) in the hot gas within a few hundred AU of the protostar. Highly excited NH_3 inversion lines at cm wavelengths also trace the same region (Goddi, Zhang & Moscadelli 2015). Such spectra provide key information about the temperature and velocity field in the vicinity of the protostars.

Hydrides, and especially water and OH, are interesting probes of protoplanetary disks, since different lines can be used to probe different regions : ground state lines trace the cold outer regions of the disk, while excited lines trace the illuminated surface closer to the central protostar. Following the first detections of water vapor in the inner region (within a few AU) (e.g. Salyk et al. 2008; Carr & Najita 2008), *Herschel*/PACS spectroscopy in the FIR has confirmed the presence of OH and H_2O in protoplanetary disks around both TTauri and Herbig AeBe stars, the latter having a higher OH/H_2O abundance ratio than the former (Fedele et al. 2013). Both ortho and para H_2O ground state lines have been detected by *Herschel*/HIFI towards TW-Hya (Hogerheijde et al. 2011). Most of the water is frozen as ice in the disk mid-plane, and water vapor represents a very minor fraction of the water reservoir. Because of the high line opacity, the interpretation of the detected signals requires a good understanding of the disk geometry and sophisticated radiative transfer calculations. Other *Herschel* detections include CH^+ tracing the UV-irradiated disk surface, and *o*-NH_3 associated with cool layers (Thi et al. 2011).

JWST: The James Webb Space Telescope, a 6.5 m telescope, operating between 0.6 and 28 μm, will be launched in late 2018.

6.1. Water and oxygen hydrides

In dense gas, water is the main oxygen hydride, together with hydroxyl radical OH, and their deuterated counterparts HDO, D_2O, OD, while the main ion is H_3O^+. While water ice is ubiquitous in molecular clouds, with a detection threshold of about 3 magnitudes of visual extinction (Whittet et al. 2013), the detection of water vapor in cold cores is very challenging because of the need of a space-borne system combining high sensitivity and high spectral resolution. Thanks to *Herschel*/HIFI, water vapor was detected towards the L1544 prestellar core (Caselli et al. 2012). The line profile shows an inverse P-Cygni profile, with a blue-shifted emission peak and a red-shifted absorption tracing the slow gravitational collapse of this core. Although the water abundance relative to H_2 is very small, $\sim 10^{-9}$, the mere presence of water vapor in such a cold ($T = 7$ K) and dense ($n(H_2) > 10^6$ cm^{-3}) environment indicates that the desorption induced by the secondary FUV photons ($\chi = 10^{-4}$, Prasad & Tarafdar 1983) produced during the interaction of cosmic rays with molecular hydrogen is efficient. This observation is consistent with predictions from chemical models such as those shown in Figure 8, where water vapor is present at a cloud depth of a few magnitudes of extinction (Hollenbach et al. 2012). In dense and cold gas, water is cycled between the gas and solid phase through H_3O^+. Hence

the water OPR is expected to deviate from thermal equilibrium in a similar way as for NH_3 (Sipilä, Caselli & Harju 2015). Observations of H_3O^+ or of its deuterated counterparts H_2DO^+, HD_2O^+ and D_3O^+ could provide further constraints on the cosmic ray ionization rate. While no detection towards cold cores has been achieved so far, several H_3O^+ lines show up in emission towards massive star forming regions tracing the presence of energetic radiation and/or cosmic rays produced by the embedded protostar (Benz et al. 2013).

Although most rotational water lines are not observable from the ground, because of the presence of water vapor in the Earth atmosphere, the transmission is good for rotational lines of heavy water. Both HDO (Beckman et al. 1982) and D_2O (Butner et al. 2007) are present with a moderate level of fractionation. The number of measurements of HDO/H_2O and D_2O/HDO abundance ratios in the same source is small. In Orion-KL, the prototypical hot-core, HDO/$H_2O \sim 3 \times 10^{-3}$, a factor of two larger than D_2O/HDO (Neill et al. 2013). Most species show a D/H ratio in the range $2 - 8 \times 10^{-3}$ in this source. As reviewed by Caselli & Ceccarelli (2012), the deuterium fractionation of water vapor is a complex phenomenon, because it is controlled by both solid-phase and gas-phase processes and is likely time-dependent given the similarity of the chemical time scales with the free fall time of dense cores. The OD radical has been detected with the SOFIA airborne observatory in the cold envelope surrounding the low mass protostar IRAS16293-2422 (Parise et al. 2012). The large OD/HDO abundance ratio (OD/HDO = 20 - 90) remains to be fully explained. The dissociative recombination of H_2DO^+ may contribute to the OD enhancement, but a quantitative assessment awaits a measurement of the branching ratios toward HDO and OD. Because of their large critical densities and upper energy levels, the sole HDO transitions detectable in cold cores are the two ground state transitions at 465 GHz ($1_{01} - 0_{00}$) and 894 GHz ($1_{11} - 0_{00}$). In hot cores and hot corinos the conditions are favorable for collisional excitation of many HDO levels, leading to a richer spectrum. For a collapsing core around a massive protostar, the HDO ground state transitions are particularly sensitive to the velocity field in the collapsing envelope while the excited lines probe the hot inner region (e.g. Coutens et al. 2014). Like H_2O, D_2O has two spin symmetry states, with p-D_2O being the more stable species. o-D_2O has its lowest rotational state at a energy 17 K above that of p-D_2O, and ortho-states have a spin degeneracy twice that of para-states. From *Herschel* observations of both p-D_2O and o-D_2O, Vastel et al. (2010) concluded that the OPR is consistent with the statistical value of 2.

6.2. Methane and carbon hydrides

As it is for oxygen hydrides, the competition between condensation and desorption is also important for carbon hydrides in dense and FUV-shielded gas. There are, however, two important differences with oxygen : *i)* the carbon reservoir is CO and not methane, *ii)* carbon hydride radicals (CH, CH_2, CH_3) and ions (CH_3^+) initiate the organic chemistry and therefore play a pivotal role in the formation of a large fraction of the molecules present in the ISM. Another interesting property of the methylidyne radical, CH, is the linear scaling of its column density, deduced from the intensity of its Λ-doubling transitions at 3.3 GHz, with that of H_2 up to $A_V \sim 3$ mag (Mattila 1986; Chastain, Cotten & Magnani 2010). Although these lines are inverted, with negative excitation temperatures, their integrated intensity approximately scales with the CH column density (Liszt & Lucas 2002). *Herschel* observations of the CH ground state rotational lines confirm this behavior: towards the low mass protostar IRAS16293-2422, CH probes the cold envelope (Bottinelli et al. 2014), while in more massive sources CH shows a combination of emission and absorption features (Gerin et al. 2010b), indicating that CH is present in the dense material. The methylene radical, CH_2, shares the same chemistry as CH. Its ground state transition has been detected by ISO (Polehampton et al. 2005) following its identification in Orion-KL (Hollis, Jewell & Lovas 1995).

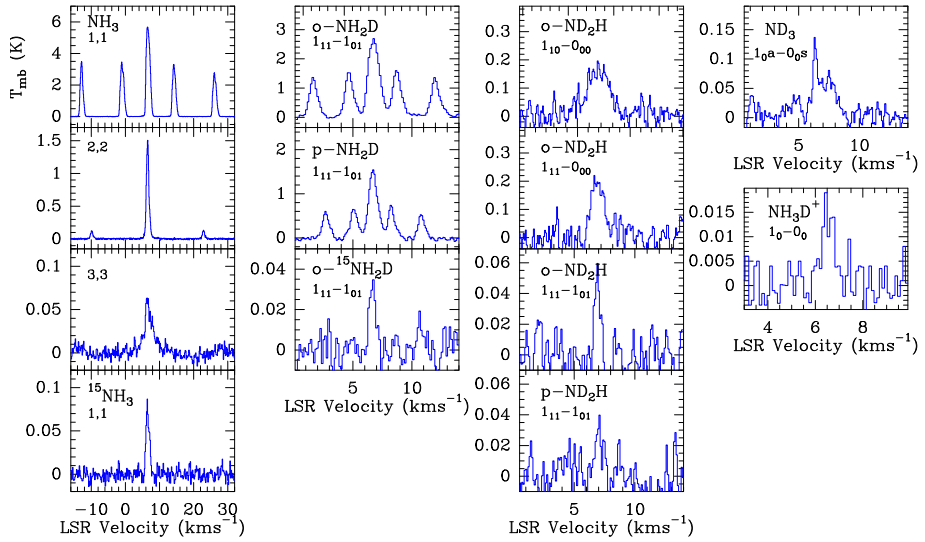

Figure 13

Ground based spectra of nitrogen hydrides towards the protostellar core Barnard1b (T = 12 K, n_{H_2} = 10^5 cm^{-3}, $N(H_2)$ = 10^{23}cm^{-2}) (adapted from Daniel et al. 2013; Lis et al. 2010b; Cernicharo et al. 2013).

Methane is best probed by infrared spectroscopy using either ground-based or space-born telescopes in the 8 μm region (Lacy et al. 1991; Öberg et al. 2008). Frozen methane has an abundance $\sim$ 5% that of water ice, supporting a formation process through sequential hydrogenation of carbon on grain surfaces. The gas phase abundance is more uncertain and ranges between 10^{-8} and 10^{-6} relative to H_2. Even for the highest abundances, most of the interstellar methane is in solid form.

Deuterium fractionation is predicted to be very efficient for carbon hydrides, since deuterated methylium CH_2D^+ is one of the main actors in enriching molecules in deuterium. CH_2D^+ is operating in lukewarm regions (T $\sim$ 30 − 70 K) where the kinetic temperature is too high for H_2D^+ to be enriched. The DCN and HDCO molecules are typical products of CH_2D^+ induced chemistry, with observed fractionation levels consistent with chemical models (Roueff et al. 2013). Unfortunately, no astronomical detection of the related species CD and CHD has been reported so far. Further tests involve the search for CH_2D^+. Its rotational spectrum has been measured by Amano (2010), and a tentative detection has been reported towards Orion-KL by Roueff et al. (2013), which awaits confirmation from observations of a less spectrally crowded region. Because of its small dipole moment of 0.3 Debye, CH_2D^+ rotational lines are weak at the predicted abundance level. Deuterated methane CH_3D has a non-zero albeit small dipole moment (0.0057 D), allowing observations of rotational transitions from the ground. After a very deep integration, Sakai et al. (2012) reported a tentative detection towards the IRAS04368+2557 protostar in the L1527 core. Further searches for CH_3D are needed to confirm this detection, which implies rather large CH_3D ($\sim 3 \times 10^{-7}$) and CH_4 ($\sim 4 \times 10^{-6}$) gas phase abundances, and very little methane left on grain mantles.

6.3. Ammonia and nitrogen hydrides

Nitrogen hydrides are mainly formed in the gas phase through a chain of hydrogen abstraction reactions starting from $N^+ + H_2 \rightarrow NH^+ + H$. This reaction is slightly endothermic (Fig. 2), and therefore is

more efficient for o-H_2 than for p-H_2. Because of the rather low formation rate in p-H_2 enriched gas, a formation route on grain surfaces has also been suggested. Subsequent hydrogen abstraction reactions $NH_n^+ + H_2 \rightarrow NH_{n+1}^+ + H$ with $n = 1, 2, 3$ followed by dissociative recombination reactions lead to the molecular ions NH_2^+, NH_3^+ and NH_4^+, and the neutral hydrides NH, NH_2 and NH_3. The detection of NH_3D^+ by Cernicharo et al. (2013) nicely confirms this theoretical scheme. NH is also formed as a secondary product of the dissociative recombination reaction of N_2H^+ (Vigren et al. 2012). In dense clouds, the abundances of nitrogen hydrides are dominated by ammonia, with NH:NH_2:NH_3 = 3:1:19 for the dense core around the protostar IRAS16293-2422 (Le Gal et al. 2014). The excess of NH over NH_2 is explained by its additional formation route from the dissociative recombination of N_2H^+.

Ammonia has two spin symmetry states, o-NH_3 with K values multiple of three and $K = 0$, and p-NH_3 for other K values. The energy difference between o-NH_3 and p-NH_3 is 21.5 K, and the high temperature value of the OPR ratio is 1, while an excess of o-NH_3 is expected at temperatures lower than 50 K. As a symmetric top with two equilibrium configurations, ammonia exhibits inversion transitions between equivalent rotational states. While the low energy NH_3 inversion transitions probe the para species, the first o-NH_3 state accessible from the ground is the $(J, K) = (3, 3)$ level at 120 K above ground. Therefore most NH_3 measurements in dense cores only trace p-NH_3, and the total ammonia column density is derived assuming an ortho-to-para ratio (OPR) of one. Using *Herschel* absorption data on o-NH_3 and p-NH_3, Persson et al. (2010) measured an anomalous value of the OPR ratio of 0.7. In p-H_2 enriched gas, the chain of ion-molecule reactions forming NH_3 favors the formation of p-NH_3 due to spin statistics selection rules (Rist et al. 2013; Faure et al. 2013). This effect could be prominent in cold cores, with predicted OPR $\sim$ 0.5 for NH_3. The deficit in o-NH_3 implies a small error in the total NH_3 column density deduced from p-NH_3 observations. The amidogen radical NH_2 is formed in the same chain of gas phase reactions as ammonia. With two identical protons, NH_2 has two spin symmetry states, the ortho state with a spin multiplicity of three is the most stable, and the para state with a spin multiplicity of one, with an energy difference of 30 K. As for ammonia, the NH_2 OPR is sensitive to the presence of an excess of p-H_2, and can reach values lower than 3, which are not permitted in thermal equilibrium, in p-H_2 enriched gas (Le Gal et al. 2014). So far only a handful of measurements of the NH_3 and NH_2 OPR are available (Persson et al. 2015). Such measurements may be able to put constraints on the H_2 OPR in dense and shielded gas.

Ammonia is a a good tracer of both prestellar and protostellar cores, with a fractional abundance relative to H_2 of $\sim 10^{-8}$ (Bergin & Tafalla 2007). It remains undepleted in the gas phase up to relatively large densities ($\sim 10^6$ cm^{-3}), in contrast to the case of CO. As illustrated in **Figure 13**, all deuterated ammonia isotopologues have been detected in the ISM : NH_2D, ND_2H and ND_3 (Roueff et al. 2005), as well as the ^{15}N variants $^{15}NH_3$ (*e.g.* Lis et al. 2010b) and $^{15}NH_2D$ (Gerin et al. 2009), and even NH_3D^+ (Cernicharo et al. 2013). The deuterated ammonia isotopologues are better tracers of the cold inner regions of prestellar cores, where most molecules are frozen onto grains, than is NH_3 itself, with fractionation levels above 10% in such regions (*e.g.* Daniel et al. 2013). The fractionation of ammonia and its precursors NH and NH_2 is most efficient at temperatures lower than $\sim$ 20 K because it involves reactions with HD, H_2D^+, D_2H^+ and D_3^+ that are enhanced at temperatures below 20 K (Roueff, Loison & Hickson 2015). ND has been detected (Bacmann et al. 2010), with [ND]/[NH] reaching $\sim$ 10 %, a value similar to that observed for [NH_2D]/[NH_3], but with a large uncertainty because of the difference in excitation between NH and ND.

At low temperatures, nitrogen may become fractionated, leading to a possible difference between the elemental isotopic ratio $^{15}N/^{14}N$ and the abundance ratio of nitrogen-bearing species. The topic is of interest because analysis of primitive solar system material as found in carbonaceous chondrites or in micro-meteorites have led to the identification of specific regions with isotopic ratios very different from the bulk, in either D/H, $^{15}N/^{14}N$ or both (Aléon 2010). The difference between the $^{15}N/^{14}N$

isotopic ratio in the Sun (and the solar system), 2.3×10^{-3}, and that of the Earth, 3.8×10^{-3}, also indicates that active fractionation processes were operating in the early solar system. Following the evolution of D/H and $^{15}N/^{14}N$ in interstellar molecules along the formation of a protostar and its circumstellar disk is therefore a means of constraining the chemical evolution of the star forming system and the formation of its primitive bodies. So far, measuring the $^{15}N/^{14}N$ isotopic ratio has proven to be much more difficult than D/H because of the large dynamical range required. Chemical models have investigated the coupled fractionation of hydrogen, carbon, and nitrogen, and also the dependence with time during the collapse. The prediction is that NH_3 should preserve within 20% the original nitrogen isotopic ratio, unlike other species such as HCN which could become highly fractionated (Wirström et al. 2012; Roueff, Loison & Hickson 2015). Selective photodissociation of N_2 as modeled by Heays et al. (2014) also plays a role in the nitrogen fractionation in protoplanetary disks.

6.4. Sulfur and other heavy element hydrides

Hydrogen sulfide H_2S is the main sulfur hydride in dense clouds, while SH and SH^+ are more confined to diffuse and translucent clouds (Neufeld et al. 2015b; Crockett et al. 2014), or the UV-illuminated cloud edges as described in Section 4. The sulfur chemistry proceeds differently from that of oxygen or carbon because the hydrogen abstraction reactions between HS_n^+ and H_2 are highly endothermic. The hydrogenation of sulfur atoms on grains, followed by desorption, is a possible chemical pathway to form hydrogen sulfide in dense cores, although no confirmed detection of H_2S ice has been reported so far. Singly and doubly deuterated hydrogen sulfide have been detected in a few dark clouds (van Dishoeck et al. 1995; Vastel et al. 2003) with a significant fractionation level of $\sim 10\%$. The fractionation is sensitive to the temperature since HDS and D_2S are not detected in hot cores, despite their large H_2S column densities. For the Orion-KL region, the upper limit for the HDS/H_2S ratio is a few 10^{-3}, at the same level as HDO/H_2O (Crockett et al. 2014).

The halogen hydrides HF and HCl are expected to be the main gas phase reservoirs of fluorine and chlorine in dense and well shielded gas (Neufeld & Wolfire 2009), and could be used to monitor the depletion of these elements. The detection of the $J = 2 - 1$ line of HF in absorption towards SgrB2 (Neufeld et al. 1997) implied a fluorine depletion close to two orders of magnitude. Surveys of hydrogen chloride also conclude that chlorine depletes on grains by at least two orders of magnitude (*e.g.* Peng et al. 2010; Kama et al. 2015). While many previous analysis relied on collisional cross sections with He, new calculations have been performed for the H_2-HCl system by Lanza et al. (2014), providing further confirmation of the low HCl abundance in dense gas. HCl may return to the gas phase in the hot inner region around massive protostars (Goto et al. 2013).

7. HYDRIDES AS DIAGNOSTIC TOOLS

Because the chemical pathways leading to the formation of interstellar hydrides are relatively simple and well-understood, the analysis of the observed abundances is relatively straightforward and provides key information about the physical and chemical conditions within the environments in which hydrides are found. Several examples have already been discussed. These include observations of CH^+ and SH^+ in diffuse molecular clouds, which trace the effects of shocks or TDRs (see Section 5), and observations of neutral hydrides such as HF, HCl and H_2O in dense clouds, which probe the depletion of heavy elements onto icy grain mantles (see Section 6 and 2). In this section, we will discuss several additional cases where observations of hydride molecules provide unique information about the ISM. In particular, we will consider how observations of specific hydrides – namely CH, H_2O, and HF – provide valuable surrogate tracers for molecular hydrogen, the dominant molecular constituent of the

ISM but one that is difficult to observe directly, while several hydride cations (including ArH^+, HCl^+, OH^+ and H_2O^+) are most abundant in *partially-molecular* gas, with each molecule predicted to show a peak abundance in material with a specific molecular fraction, f_{H_2} We will also discuss how hydride molecules can measure the cosmic-ray (or X-ray) ionization rate in the Milky Way and other galaxies.

7.1. Hydride as tracers of H_2

Although it is the primary molecular constituent of the ISM, H_2 is hard to detect because it lacks a permanent dipole moment. Absorption line observations of the ultraviolet (and dipole-allowed) Lyman and Werner bands of H_2 measure the H_2 column density directly, although they are limited to relatively unreddened lines-of-sight toward relatively nearby hot stars (e.g. Rachford et al. 2009). Absorption in the near-infrared quadrupole-allowed vibrational bands has also been observed toward a few highly-embedded infrared sources (Lacy et al. 1994; Kulesa 2002), but is an extremely insensitive probe (in that very large H_2 column densities are needed to generate even very small optical depths). There has therefore been a considerable effort to identify surrogate observational tracers that can be used to measure H_2 column densities and masses. Observations of CO emission have been widely used to measure H_2 masses (Bolatto, Wolfire & Leroy 2013, and references therein), but fail to trace a significant component of the molecular ISM. This component has been called the "CO-dark" or "CO-faint" molecular gas (Grenier, Casandjian & Terrier 2005; Wolfire, Hollenbach & McKee 2010; Bolatto, Wolfire & Leroy 2013), and consists of material that is sufficiently shielded from UV radiation to have a substantial H_2 fraction but not so well-shielded as to contain abundant CO. This material lies at the transition between diffuse and translucent clouds near $A_V = 1$ mag (e.g. van Dishoeck 1998).

Three hydride molecules – CH, H_2O, and HF – exhibit remarkably constant abundance ratios relative to H_2, and are therefore valuable as surrogate tracers that are sensitive to CO-dark gas. The best studied case is CH, for which optical absorption-line observations can be calibrated with respect to UV absorption-line observations of H_2, yielding N(CH) and $N(H_2)$ column densities for sight-lines with $N(H_2)$ in the range $\sim 10^{19}$ to $\sim 10^{21}\mathrm{cm}^{-2}$ (e.g. Sheffer et al. 2008). The observed $N(\mathrm{CH})/N(H_2)$ ratio has a mean of 3.5×10^{-8}, shows a dispersion of 0.21 dex, and exhibits no dependence on $N(H_2)$; moreover, the $N(\mathrm{CH})/N(H_2)$ can be determined for sight-lines of even larger $N(H_2)$ – albeit less directly through a comparison of cm-wavelength CH emission with reddening measurements – and is found to remain entirely consistent with the $N(H_2) \lesssim 10^{21}\mathrm{cm}^{-2}$ value for H_2 column densities up to $\sim 4 \times 10^{21}\mathrm{cm}^{-2}$ (Mattila 1986; Liszt & Lucas 2002). State of the art steady-state chemical models reproduce the observed trend between CH and H_2 correctly for densities larger than 100 cm^{-3}, while for lower densities the CH production is closely related to that of CH^+, as explained in Sect 5.

Observations of submillimeter absorption, performed with the HIFI instrument on *Herschel* have extended the use of hydrides as probes of $N(H_2)$, providing access to the $N = 1, J = 3/2 \rightarrow 1/2$ CH Λ-doublet at 532/536 GHz along with rotational transitions out of the ground-state of the neutral hydrides HF and H_2O. Such observations show the $N(\mathrm{HF})/N(\mathrm{CH})$ ratio to be remarkably constant in diffuse clouds, with a typical value of 0.4, implying a mean $N(\mathrm{HF})/N(H_2)$ ratio of 1.4×10^{-8}, given a $N(\mathrm{CH})/N(H_2)$ ratio of 3.5×10^{-8}. In the limit where $f_{H_2} \sim 1$, this $N(\mathrm{HF})/N(H_2)$ ratio implies that HF accounts for $\sim 40\%$ of the gas-phase fluorine. A direct measurement of the $N(\mathrm{HF})/N(H_2)$ column density ratio in the diffuse ISM has been obtained (Indriolo et al. 2013) toward a single source, the hot star HD 154368, by combining observations of the near-IR $v = 1 - 0$ $R(0)$ HF *vibrational* transition with those of dipole-allowed UV transitions of H_2 . This measurement provided an independent and entirely consistent ($1.15 \pm 0.41 \times 10^{-8}$) determination of the $N(\mathrm{HF})/N(H_2)$ ratio. Originally, the predictions of astrochemical models by Neufeld & Wolfire (2009) for fluorine-bearing interstellar molecules predicted a $N(\mathrm{HF})/N(H_2)$ ratio roughly twice as large as the observed value. However, recent labo-

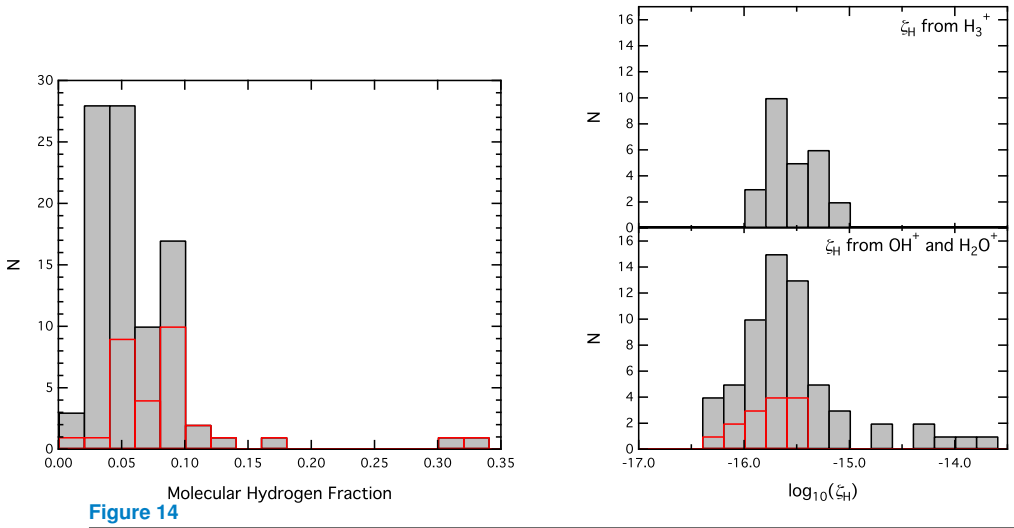

Figure 14

Distributions of molecular hydrogen fraction, f_{H_2} (left panel) and cosmic-ray ionization rate, ζ_H (lower right panel), inferred from *Herschel* observations of OH^+ and H_2O^+ and reproduced from Indriolo et al. (2015). The red histogram applies to material with line-of-sight velocities within 5 km s^{-1} of the systemic velocity of the background source (i.e. to material that may be in the vicinity the continuum source). The upper right panel shows the distribution of cosmic-ray ionization rates inferred (for a different set of sight-lines) from observations of H_3^+.

ratory measurements (Tizniti et al. 2014) of the rate coefficient for the reaction of H_2 with F to form HF appear to have revealed the source of the discrepancy: the original astrochemical models adopted a theoretical value for the rate coefficient at low temperature that was a significant overestimate. Revised models that assume instead the laboratory-measured value for the rate of HF formation predict $N(HF)/N(H_2)$ ratios in good agreement with the astronomical observations.

Another neutral hydride that has been extensively observed with *Herschel*, H_2O, is a third potential H_2 tracer within the diffuse ISM. The mean $N(H_2O)/N(HF)$ ratio determined from *Herschel* observations of the diffuse ISM is 1.73 (Sonnentrucker et al. 2015), and the standard deviation is 0.87, implying a typical $N(H_2O)/N(H_2)$ ratio of 2.4×10^{-8}. The variation in the H_2O abundance is apparently somewhat larger than those in the CH and HF abundances.

Taken together, submillimeter absorption line observations of CH, H_2O and HF provide a valuable toolset for the determination of $N(H_2)$. Their column densities lie in the average ratio $N(CH) : N(H_2O) : N(HF) = 2.5 : 1.7 : 1.0$. For the spectral lines that have been most extensively observed in absorption – the 536 GHz $N = 1, J = 3/2 \rightarrow 1/2$ transition of CH, the 1113 GHz $1_{11} - 0_{00}$ transition of p-H_2O, and the 1232 GHz $J = 1 - 0$ transition of HF – the corresponding ratio of velocity-integrated optical depths is 0.26:0.6:1.0. Thus, the HF transition provides the most sensitive probe of H_2 along any sight-line, followed by H_2O and CH. These probes are complementary because in cases where the HF absorption is optically-thick, yielding only a lower limit on the column density, the CH absorption is often optically-thin. Conversely, absorption features that are too weak to detect in observations of CH may be detectable in observations of HF. While CH, HF and H_2O, can be regarded as "primary" tracers of molecular hydrogen, their column densities are well correlated with other, non-hydride molecules that can be detected from the ground at millimeter wavelengths, including HCO^+ (*e.g.* Lucas & Liszt 1996) and C_2H (Lucas & Liszt 2000; Gerin et al. 2010b). Absorption line observations of these non-hydride "secondary" tracers can also be used to estimate $N(H_2)$, albeit with lower accuracy. OH can

be added to the list of the "secondary" tracers, given the excellent correlation between the opacities of the HCO^+ $J = 1 \rightarrow 0$ and OH 1665 & 1667 MHz *absorption* lines (Liszt & Lucas 1996), and the moderate scatter in the OH/H_2O column density ratio (Wiesemeyer et al. 2015).

Along with absorption line observations of CH, HF, and H_2O, observations of CH and OH *emission* show considerable promise as a probe of CO-dark molecular gas (Liszt & Lucas 1996). This promise has been demonstrated recently by Allen, Hogg & Engelke (2015), who performed a sparse, high-sensitivity pilot survey near the Galactic plane for the 18 cm emission lines of OH: fewer than one-half of the multiple spectral features thereby detected were accompanied by detectable CO line emission. Further investigations, both observational and theoretical, will be needed to make quantitative use of this H_2 tracer.

7.2. Probes of the molecular fraction

While the neutral hydrides CH, HF and H_2O are most abundant in gas with a large molecular fraction, f_{H_2}, several molecular ions show peak abundances in material with a smaller H_2 fraction. This behavior is particularly notable for ions that are destroyed rapidly by reaction with H_2: these include ArH^+, which is destroyed by proton transfer to H_2 (Schilke et al. 2014), and OH^+ and H_2O^+, which undergo H-atom abstraction reactions to form H_2O^+ and H_3O^+ respectively. The $n(OH^+)/n(H_2O^+)$ ratio is a particularly valuable probe of the H_2 fraction (Neufeld et al. 2010), because the reaction of H_2 with OH^+, which forms H_2O^+, competes with dissociative recombination of OH^+ with electrons; thus, the $n(OH^+)/n(H_2O^+)$ ratio is larger in regions of small f_{H_2} and smaller in regions of large f_{H_2}. Through an analysis of 92 OH^+ and H_2O^+ absorption features detected by *Herschel* along the sight-lines to 20 bright Galactic continuum sources, Indriolo et al. (2015) obtained the histogram of f_{H_2} values reproduced in **Figure 14 (left panel)**. This analysis clearly reveals a substantial amount of interstellar gas with a molecular hydrogen fraction of a few percent. Of course, because the observations measure a ratio of column densities rather than volume density (i.e. $N(OH^+)/N(H_2O^+)$ rather than $n(OH^+)/n(H_2O^+)$), the f_{H_2} values thereby derived are really averages over the material *that contributes most to the* OH^+ *and* H_2O^+ *absorption.* These f_{H_2} values may therefore differ substantially from those derived for the entire sight-line from a comparison of $N(H_2)$ and $N(H)$.

The argonium ion, ArH^+, traces material of even smaller f_{H_2}. Because the dissociative recombination of ArH^+ is unusually slow, reactions with H_2 become the dominant destruction mechanism for $f_{H_2} \gtrsim 10^{-4}$ and the ArH^+ abundance starts to drop once f_{H_2} increases beyond that value. Thus, as discussed by Schilke et al. (2014), ArH^+ serves as a unique probe of material that is *almost purely atomic*. This prediction for the behavior of ArH^+ is supported by the observational finding that the distribution of ArH^+ is entirely different from that of the other interstellar hydrides (see Figures 5 and 6 in Section 3 above).

7.3. Probes of the cosmic-ray ionization rate

Unlike the formation of CH^+ and SH^+, which is driven by shocks or turbulent dissipation or enhanced in strongly FUV-irradiated gas, the formation of ArH^+, OH^+ and H_2O^+ is initiated by cosmic-rays. ArH^+ formation is driven by the cosmic-ray ionization of atomic argon, with then reacts with H_2 to form ArH^+; in the case of OH^+ and H_2O^+ formation, the cosmic-ray ionization of H (or H_2, in material of large f_{H_2}) is the process that initiates the relevant reaction chain. Observations of the abundances of OH^+ and H_2O^+ in diffuse clouds, supported by detailed astrochemical calculations (Hollenbach et al. 2012), have been used to measure the cosmic-ray ionization rate in the Milky Way galaxy (Gerin et al. 2010a; Neufeld et al. 2010; Indriolo et al. 2015).

Indriolo et al. (2015) performed an analysis of all the relevant data available from *Herschel* to obtain the histogram reproduced in Figure 14 (lower right panel), which shows the distribution of cosmic-ray ionization rates in the disk of the Milky Way, ζ_H, defined here as the total rate of ionization per H atom. This quantity shows a log-normal distribution, with $\log_{10}\zeta_H$ having a mean of –15.75 (corresponding to $\zeta_H = 1.8 \times 10^{-16}\,s^{-1}$) and standard deviation 0.29. The results for ζ_H obtained from OH^+ and H_2O^+ are considerably larger than the canonical values adopted for diffuse clouds by most authors prior to 2002, but are in good agreement with estimates (*e.g.* Indriolo & McCall 2012) derived (for different sight-lines) from mid-IR observations of H_3^+. The upper right panel in Figure 14 shows the distribution of ζ_H derived from recent H_3^+ observations.

The ionization rates inferred for material in the Galactic Center are typically 10 – 100 times as large as the average value inferred for gas in the disk, and even larger ionization rates (exceeding $10^{-13}\,s^{-1}$) have been derived for circumnuclear regions within the ULIRGs Arp 220 and NGC 4418 (González-Alfonso et al. 2013). Because ionization by hard X-rays has similar effects on the chemistry as those of cosmic-ray ionization, it is not possible to unambiguously discriminate between these two possible ionization sources based on observations of hydrides alone.

7.4. Other diagnostic uses

In addition to those diagnostics that may be exploited by an analysis of hydride *chemistry*, observations of hydrides offer other tools that measure key parameters of the interstellar environment. The oblate symmetric top molecules NH_3 and H_3O^+ can provide physical probes of the gas temperature. For such molecules, the lowest states of a given quantum number K are metastable (and have a total angular momentum quantum number $J = K$). These metastable states do not undergo radiative decay, and thus their relative populations are determined by non-radiative processes. For low-lying metastable states of NH_3 and H_3O^+, the relative populations are determined by collisional excitation and probe the kinetic temperature of the gas, providing a "molecular cloud thermometer" (e.g. Walmsley & Ungerechts 1983). In the case of high-lying metastable states, however, the effects of "formation pumping" may complicate the interpretation of the observations (e.g. Lis et al. 2014).

The Zeeman splitting of hydride spectral lines offers another important diagnostic tool that has been used to estimate the interstellar magnetic field strength. The paramagnetic OH radical is of particular value, and absorption line observations of its 18 cm transitions have been used to determine the magnetic field in interstellar gas with densities in the range $n_H \sim 10^2\,cm^{-3}$ to $\sim 10^4\,cm^{-3}$ (e.g. Crutcher 2012, for a review). This material is intermediate between the lower density gas probed by HI Zeeman measurements and the higher density gas probed by CN Zeeman measurements. At yet higher densities, the Zeeman splitting of OH and H_2O *maser* transitions has been used to measure magnetic field strengths, in extreme cases revealing fields in excess of 100 mG.

Because the 22 GHz water maser emissions from shocked regions can be extraordinarily bright, they may be observed by means of Very Long Baseline Interferometry (VLBI), providing sub-milliarcsecond resolution and the possibility of measuring parallaxes and proper motions with accuracies of $\sim 10\,\mu as$ and $\sim 100\,\mu as\,yr^{-1}$ respectively (*e.g.* Reid et al. 2009; Honma et al. 2012). Such measurements provide uniquely valuable probes of fundamental Galactic parameters such as the distance to the Galactic Center and the circular rotation speed at the solar circle.

Finally, observations of hydride isotopologues can be used to determine elemental isotope ratios, which – in turn – can provide constraints upon the star formation history and the chemical evolution. In the diffuse ISM, for example, where fractionation is generally believed to be unimportant for isotopes of elements other than hydrogen or carbon, observations of $H_2^{35}Cl^+$ and $H_2^{37}Cl^+$ have been used to determine the $^{35}Cl/^{37}Cl$ isotopic ratio, both in the Galactic disk (Neufeld et al. 2015a, and references

therein) and in the redshift 0.89 absorber in front of the lensed blazar PKS 1830-211 (Muller et al. 2014a, see Section 8 below). All these determinations are entirely consistent with the solar system $^{35}Cl/^{37}Cl$ isotopic ratio of 3.1 (Lodders 2003).

8. HYDRIDES IN EXTERNAL GALAXIES

As relatively abundant and ubiquitous species, hydrides are detected in external galaxies, from local objects up to high redshift systems. The list of species includes water vapor (Yang et al. 2013; Omont et al. 2013), OH, and the related ions H_3O^+, H_2O^+ and OH^+; NH_3, CH and CH^+, as well as HF and the chlorine bearing species HCl and H_2Cl^+ (van der Werf et al. 2010; Rangwala et al. 2011, 2014; González-Alfonso et al. 2012, 2013; Kamenetzky et al. 2012; Muller et al. 2014a,b). The hydride diagnostic capabilities can be exploited to probe the physical conditions, turbulence and radiation field including X-rays and cosmic rays in a more extreme range than what is found in the Milky Way.

8.1. Local galaxies

FIR spectroscopy, performed first with *ISO*, then with *Herschel* revealed a diversity of spectral lines, especially from hydrides that accompany the set of CO rotational lines and of atomic fine structure lines. In local galaxies ($z < 0.1$), the strongest rotational lines of water vapor are the $2_{02} - 1_{11}$ and $3_{21} - 3_{12}$ transitions with rest frequencies 987.9 and 1162.9 GHz. Their luminosities are linearly correlated with the far infrared luminosity, L_{FIR}, across a broad range of infrared luminosities, $1 - 300 \times 10^{10}$ $L_\odot$, i.e. from normal galaxies up to very active starburst (Yang et al. 2013). Radiative transfer models show that FIR pumping is an important source of excitation for most H_2O lines, except for those connected to the ortho or para ground states. Fully resolved line profiles have been obtained with HIFI, showing the complexity of the line profiles even in nearby galaxies : towards M82, different H_2O lines have different line profiles ranging from pure absorption to pure emission (Weiß et al. 2010).

At moderate spectral resolution (~ 200 kms^{-1}), submm and FIR hydride lines appear in emission, in absorption or even with P-Cygni profiles. In galaxies hosting a compact starburst or an active galactic nucleus (AGN) the FIR radiation from the hot dust is pumping the rotational levels, leading to a variety of line profiles revealing the conditions close to the heavily buried compact source (van der Werf et al. 2010). OH lines from excited levels are especially interesting because they trace powerful outflows of molecular material (Sturm et al. 2011; González-Alfonso et al. 2012), that represent an important source of negative feedback in starburst galaxies or AGNs. In an analysis of 29 galaxies, González-Alfonso et al. (2015) clearly show that the OH 65μm equivalent width probes the fraction of infrared luminosity produced by a compact and warm source, i.e. is closely related to the presence of an heavily buried active region, which could escape detection otherwise. Absorption from excited levels of other hydrides like water vapor, OH^+ and H_2O^+ can also be detected. H_3O^+ deserves a special treatment. Toward the compact infrared galaxies Arp 220 and NGC 4418, absorption from H_3O^+ lines tracing the metastable levels of this symmetric top molecule are detected up to energies of ~ 1300 K. As for the Galactic sources SgrB2 and W31C, these lines trace the formation process of H_3O^+ and can therefore be used to accurately infer the ionization rate which reaches $\zeta_H > 10^{-13}$ s^{-1} in both NGC 4418 and Arp 220, as compared with the mean value in the Galactic disk of $\zeta_H = 2 \times 10^{-16}$ s^{-1} (Indriolo et al. 2015). Non metastable lines of H_3O^+ are accessible from the ground, the strongest being the $3_2^+ - 2_2^+$ line at 364 GHz (Aalto et al. 2011).

In external galaxies hydrides are important probes of the diffuse clouds, not radiating in CO. For instance Appleton et al. (2013) report the detection of water vapor in the large shock of the Stephan's Quintet, a group of five interacting galaxies. The ground state *p*-H_2O transition is the brightest sub-

AGN: An Active Galactic Nucleus is a compact region near the center of a galaxy, which is emitting intense radiation, as the result of accretion of matter on a super-massive black hole.

Starburst galaxy: A starburst galaxy is a galaxy forming stars at a rate much higher than the average. Instead of a few $M_\odot yr^{-1}$, the star formation rate can reach up to 10^3 $M_\odot yr^{-1}$.

millimeter emission line detected in this system, excluding the FIR structure lines [CII] at 158 μm and [OI] at 63 μm. The current generation of high resolution spectrometers operating in the visible allows measurement of CH, CH^+ and CN absorption lines towards stars in nearby galaxies. In the Magellanic clouds, the relationships between CN, CH, CH^+, NaI and KaI are generally consistent with those of the Milky Way but the overall CH abundance relative to H_2 is more variable, likely because of the broad range of physical conditions encountered along such sight-lines and the lower carbon abundance (Welty et al. 2006). The supernova SN2014J in M 82 (Ritchey et al. 2015) provided a bright enough background target to probe the ISM properties in the Galaxy and in M82 along this sight-line. The enhanced CH^+/CH ratio may indicate an enhanced level of turbulence in this actively star forming galaxy.

XDR: X-Ray Dominated Region

8.2. Active Galactic Nuclei : XDR prototypes

When molecular gas is exposed to intense X-ray radiation, a specific chemistry can develop. As compared with photodissociation regions, X-ray dominated regions (XDR) show longer columns of warm molecular gas because X-rays can penetrate longer columns than UV photons. Because of the increased ionization rate due to X-rays, and the higher gas temperature, some molecular abundances are modified. This is particularly the case for the oxygen hydrides OH^+, H_2O^+ and H_3O^+. In dense gas illuminated by X-rays, these species are predicted to present strong emission features, because of the increased excitation by the high electron density. The close environment of the super-massive accreting black hole in an AGN can be considered as an X-ray dominated region, even though some active galaxies also host starbursts. XDRs also exist in the close vicinity of protostars and have been modeled, for example by Stäuber et al. (2005). The *Herschel*/SPIRE spectrum of the Mrk 231 galaxy, an AGN template, shows prominent OH^+ and H_2O^+ rotational lines in emission (van der Werf et al. 2010). Other species sensitive to high X-ray irradiation are atomic carbon, H_3^+, H_2O and HCN. Because S^{2+} reacts rapidly with H_2, producing SH^+ among other species, Abel, Federman & Stancil (2008) have proposed that SH^+ could be an excellent XDR tracer. This work remains qualitative because the reaction branching ratio towards SH^+ is not known. A further exploration of the reactivity of doubly ionized ions with H_2 (e.g. C^{2+}) and of the branching ratios towards hydrides is needed to support this new chemical route.

8.3. High redshift galaxies

Hydride lines at THz rest frequencies are redshifted into the (sub)millimeter range and become accessible to the ALMA and NOEMA (NOrthen Extended Millimeter Array) interferometers , offering new diagnostic capabilities of the conditions in high redshift galaxies. **Figure 15** shows the ground state hydride lines accessible to ALMA with the corresponding redshift range. For water vapor, excited lines are also easily detected (Omont et al. 2013), with line strength only a factor two to three lower than CO. Nevertheless, the detection of water vapor at high redshift was achieved about two decades after that of CO, largely because the limited band-width of available receivers prohibited searching over a broad frequency ranges. As the CO rotational line frequencies are relatively distant from the strongest water line frequencies, targeting CO meant avoiding H_2O until recently. The tight correlation of the H_2O line luminosity with the FIR luminosity may be used to derive the star formation rate.

Towards gravitationally lensed QSOs, the gas of the lensing galaxy may produce absorption lines on the continuum of the background object. The sight-line towards the radio loud QSO PKS1830-211 is particularly rich, with numerous absorption lines detected toward the two main images, sampling two lines of sight in the lensing galaxy at z = 0.89. ALMA observations enabled the detection of the same hydride lines that were seen in the Milky Way by *Herschel* (Muller et al. 2014b,a). Other high

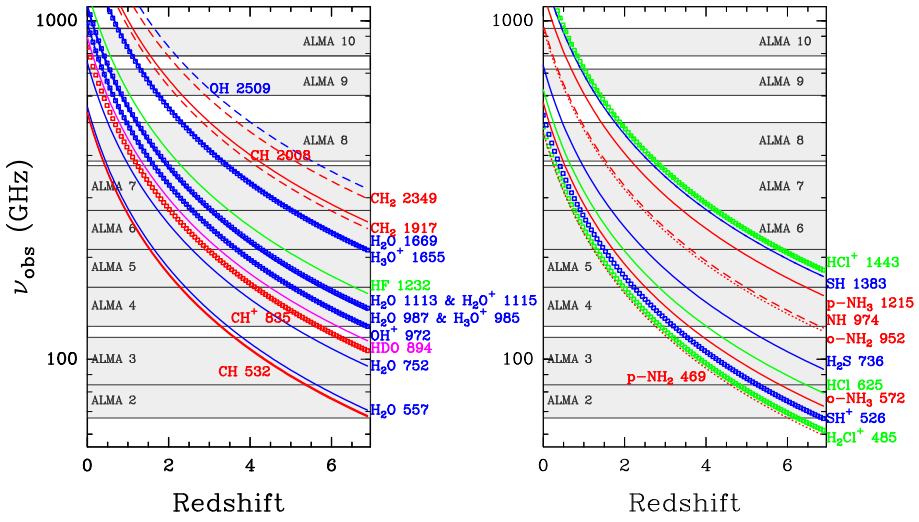

Figure 15

Frequencies of the ground state transitions of the main hydrides as a function of redshift. Some rotationally excited lines of water vapor are also included. Molecular ions are shown with squares. On the left panel, oxygen-bearing species are displayed in blue, carbon-bearing species in red, and halogens in green. On the right panel, nitrogen-bearing species are shown in red, sulfur-bearing species in blue and halogens in green. ALMA bands 2 to 10 are indicated in grey.

redshift hydride detections include H_2O^+ in a bright submillimeter galaxy (Weiß et al. 2013), CH in the average spectrum of 22 such objects (Spilker et al. 2014), CH^+ in the optical afterglow spectrum of the gamma ray burst GRB 145050A at z=0.89 (Fynbo et al. 2014) and in three hyper luminous galaxies (Falgarone et al. 2015).

While the same species are detected at $z \sim 1$ as in the Milky Way, some hydrides may become undetectable at higher redshift because of the lack of the corresponding chemical element. For instance HF has been tentatively detected in Cloverleaf QSO at $z = 2.56$ (Monje et al. 2011) but not in the higher redshift source APM 08279+5255 at $z = 3.89$ (Lis et al. 2011). The absence of HF is best explained by a low fluorine abundance, since the same source exhibits bright CO and H_2O lines.

The comparison of carefully selected hydride line profiles provides an interesting test of the variation of two fundamental constants with time, the fine structure constant $\alpha = e^2/\hbar c$ and the proto-to-electron mass ratio $\mu = m_p/m_e$. The sensitivity of the CH doublet at 532/536 GHz to variations in α and μ have been computed by de Nijs, Ubachs & Bethlem (2012). These lines can be observed simultaneously with the $1_{10} - 1_{01}$ transition of o-H_2O, reducing the systematic effects when comparing lines at very different frequencies, and therefore are complementary to other diagnostics like NH_3, CH_3OH and H_2 discussed by Jansen, Bethlem & Ubachs (2014).

9. CONCLUSIONS AND FUTURE PROSPECTS

Since their first discovery in the diffuse interstellar medium, hydrides have been proven to exist in the wide variety of interstellar and circumstellar environments, from the most diffuse, almost purely atomic regions, up to dense cores and protoplanetary disks. Given the relative simplicity of their chemistry, and the good level of understanding of their formation processes, the diagnostic properties

of hydrides need to be further explored in the future, taking advantage of the increasing capabilities of high spectral resolution spectrometers from UV-visible up to centimeter wavelengths. As shown in Figure 15, hydrides ground state transitions, which are mostly not accessible from ground based observatories, are redshifted to spectral regions with better atmospheric transmission in distant galaxies, where ALMA and NOEMA are operating. This offers diagnostics of the presence of molecular hydrogen, cosmic ray ionization rate, elemental abundances as well as dynamical processes in the forms of shocks, turbulence and large scale winds, from the local interstellar medium up to the most distant galaxies. The combined increase in sensitivity and spectral resolution will enable more accurate measurements of isotopic ratios, with a focus on deuterium and nitrogen, as a means to understand the origin of volatiles in the solar system, and more generally the formation of planets in circumstellar disks. It will be exciting to connect the ISM information with the measurements performed on the 67P/Churyumov-Gerasimenko comet by the Rosetta spacecraft.

At longer wavelengths, the development of powerful instruments at centimeter wavelengths offers interesting possibilities for accessing the Λ-doubling transitions of OH (both in the ground state and in excited levels), CH and the inversion transitions of NH_3, and for comparing the distribution of these species with that of atomic hydrogen at unprecedented sensitivity and spatial resolution. At shorter wavelengths, the launch of the JWST, and the construction of the next generation of ground-based telescopes, will provide new tools for studying the relation between ices and gas phase species, especially water, methane and associated radicals.

To obtain the best results from these upcoming facilities, several scientific issues remain to be addressed in the fields of astrochemistry and molecular physics. On the astrophysics side, a significant issue is the understanding of non equilibrium processes on the abundance and excitation of the main hydrides. As described above, for a reactive hydride like CH^+, both the large scale and small scale dynamics of the media, their multi-phase structure, as well as the details of the formation and excitation process all contribute to the production and excitation. A related topic is the understanding of the hydride OPR, and how these relate to the H_2 OPR. This requires investigations of the reaction mechanisms leading to the hydride formation and destruction, taking the spin symmetry states into account, as well as more accurate astronomical measurements.

The field of laboratory astrophysics is developing fast. The interplay between the gas phase and the solid phase is a key area for progress. With their formation through hydrogen abstraction reactions, hydride abundances are particularly sensitive to rates of the dissociative recombination of molecular ions. The new cryogenic storage ring (CSR) in Heidelberg should provide measurements of the dissociative recombination rate of rotationally cold ions such as OH^+. Other exciting developments in laboratory astrophysics include deeper studies of the interaction of ices with FUV and energetic radiation using synchrotron radiation sources, particle bombardment simulating cosmic ray irradiation, and advanced theoretical calculations of molecular processes. Close collaborations between molecular physicists and astronomers will remain a key asset in this area, as it has been in the past decades.

ACKNOWLEDGMENTS

We thank M. Agúndez, J. Black, B. Godard, D. Hollenbach, N. Indriolo, E. Falgarone, S. Federman, H. Liszt, P. Sonnentrucker, E. Roueff, and M. Wolfire for a critical reading of an early version of the manuscript, and our editor E. van Dishoeck for her detailed comments and relevant suggestions. We owe a special thank to M. Agúndez, E. Dartois, B. Godard, F. Levrier, Z. Nagy, and C. Persson for help with the preparation of some figures. The work of D.A.N. has been supported by a grant issued by NASA's Jet Propulsion Laboratory for the analysis of Herschel data, and a grant from NASA's Astrophysics Data Analysis Program (ADAP). JRG thanks the Spanish MINECO and the ERC for support

under grants AYA2012-32032 and ERC-2013-Syg-610256-NANOCOSMOS. MG thanks the INSU CNRS program PCMI, and CNES for support. Figures 1, 7 left, 8, 9, 10 and 14 are reproduced with permission from AAS managed by IOP publishing ©AAS. Figures 7 right, 11 and 12 are reproduced with permission from Astronomy & Astrophysics, ©ESO.

LITERATURE CITED

Aalto S, Costagliola F, van der Tak F, Meijerink R. 2011. *Astron. Astrophys.* 527:A69
Abel NP, Federman SR, Stancil PC. 2008. *Astrophys. J., Lett.* 675:L81–L84
Agúndez M, Goicoechea JR, Cernicharo J, Faure A, Roueff E. 2010. *Astrophys. J.* 713:662–670
Alata I, Cruz-Diaz GA, Muñoz Caro GM, Dartois E. 2014. *Astron. Astrophys.* 569:A119
Aleman I, Ueta T, Ladjal D, Exter KM, Kastner JH, et al. 2014. *Astron. Astrophys.* 566:A79
Aléon J. 2010. *Astrophys. J.* 722:1342–1351
Allen RJ, Hogg DE, Engelke PD. 2015. *Astron. J.* 149:123
Allers KN, Jaffe DT, Lacy JH, Draine BT, Richter MJ. 2005. *Astrophys. J.* 630:368–380
Amano T. 2010. *Astron. Astrophys.* 516:L4
Appleton PN, Guillard P, Boulanger F, Cluver ME, Ogle P, et al. 2013. *Astrophys. J.* 777:66
Arasa C, Koning J, Kroes GJ, Walsh C, van Dishoeck EF. 2015. *Astron. Astrophys.* 575:A121
Bacmann A, Caux E, Hily-Blant P, Parise B, Pagani L, et al. 2010. *Astron. Astrophys.* 521:L42
Barlow MJ, Swinyard BM, Owen PJ, Cernicharo J, Gomez HL, et al. 2013. *Science* 342:1343–1345
Bates DR, Spitzer Jr. L. 1951. *Astrophys. J.* 113:441
Batrla W, Wilson TL. 2003. *Astron. Astrophys.* 408:231–235
Beckman JE, Watt GD, White GJ, Phillips JP, Frost RL, Davis JH. 1982. *MNRAS* 201:357–364
Benz AO, Bruderer S, van Dishoeck EF, Stäuber P, Wampfler SF. 2013. *Journal of Physical Chemistry A* 117:9840–9847
Benz AO, Bruderer S, van Dishoeck EF, Stäuber P, Wampfler SF, et al. 2010. *Astron. Astrophys.* 521:L35
Bergin EA, Tafalla M. 2007. *Ann. Rev. Astron. Astrophys.* 45:339–396
Black JH. 1998. *Faraday Discussions* 109:257
Black JH, Dalgarno A. 1976. *Astrophys. J.* 203:132–142
Black JH, Dalgarno A. 1977. *ApJS* 34:405–423
Black JH, van Dishoeck EF. 1987. *Astrophys. J.* 322:412–449
Blake GA, Keene J, Phillips TG. 1985. *Astrophys. J.* 295:501–506
Bolatto AD, Wolfire M, Leroy AK. 2013. *Ann. Rev. Astron. Astrophys.* 51:207–268
Boogert ACA, Gerakines PA, Whittet DCB. 2015. *Ann. Rev. Astron. Astrophys.* 53:541–581
Boonman AMS, Doty SD, van Dishoeck EF, Bergin EA, Melnick GJ, et al. 2003. *Astron. Astrophys.* 406:937–955
Bottinelli S, Wakelam V, Caux E, Vastel C, Aikawa Y, Ceccarelli C. 2014. *MNRAS* 441:1964–1973
Bron E, Le Bourlot J, Le Petit F. 2014. *Astron. Astrophys.* 569:A100
Bruderer S, Benz AO, Stäuber P, Doty SD. 2010. *Astrophys. J.* 720:1432–1453
Butner HM, Charnley SB, Ceccarelli C, Rodgers SD, Pardo JR, et al. 2007. *Astrophys. J., Lett.* 659:L137–L140
Carr JS, Najita JR. 2008. *Science* 319:1504–
Carruthers GR. 1970a. *Astrophys. J., Lett.* 161:L81
Carruthers GR. 1970b. *Astrophys. J., Lett.* 161:L81
Caselli P, Ceccarelli C. 2012. *The Astron. Astrophys. rev.* 20:56
Caselli P, Keto E, Bergin EA, Tafalla M, Aikawa Y, et al. 2012. *Astrophys. J., Lett.* 759:L37
Cazaux S, Tielens AGGM. 2004. *Astrophys. J.* 604:222–237
Cernicharo J, Liu XW, González-Alfonso E, Cox P, Barlow MJ, et al. 1997. *Astrophys. J., Lett.* 483:L65–L68
Cernicharo J, Tercero B, Fuente A, Domenech JL, Cueto M, et al. 2013. *Astrophys. J., Lett.* 771:L10
Chastain RJ, Cotten D, Magnani L. 2010. *Astron. J.* 139:267–278
Chernoff DF, McKee CF, Hollenbach DJ. 1982. *Astrophys. J., Lett.* 259:L97–L101
Cheung AC, Rank DM, Townes CH, Thornton DD, Welch WJ. 1968. *Physical Review Letters* 21:1701–1705
Cheung AC, Rank DM, Townes CH, Thornton DD, Welch WJ. 1969. *Nature* 221:626–628

Choi Y, van der Tak FFS, Bergin EA, Plume R. 2014. *Astron. Astrophys.* 572:L10
Coutens A, Vastel C, Hincelin U, Herbst E, Lis DC, et al. 2014. *MNRAS* 445:1299–1313
Crane P, Lambert DL, Sheffer Y. 1995. *Astrophys. J. Suppl.* 99:107
Crockett NR, Bergin EA, Neill JL, Black JH, Blake GA, Kleshcheva M. 2014. *Astrophys. J.* 781:114
Crutcher RM. 2012. *Ann. Rev. Astron. Astrophys.* 50:29–63
Daniel F, Dubernet ML, Grosjean A. 2011. *Astron. Astrophys.* 536:A76
Daniel F, Faure A, Dagdigian PJ, Dubernet ML, Lique F, Forêts GPd. 2015. *MNRAS* 446:2312–2316
Daniel F, Gérin M, Roueff E, Cernicharo J, Marcelino N, et al. 2013. *Astron. Astrophys.* 560:A3
Dartois E, Cox P, Roelfsema PR, Jones AP, Tielens AGGM, et al. 1998. *Astron. Astrophys.* 338:L21–L24
De Luca M, Gupta H, Neufeld D, Gerin M, Teyssier D, et al. 2012. *Astrophys. J., Lett.* 751:L37
de Nijs AJ, Ubachs W, Bethlem HL. 2012. *Phys. rev. A* 86:032501
Douglas AE, Herzberg G. 1941. *Astrophys. J.* 94:381
Draine BT, Katz N. 1986. *Astrophys. J.* 310:392–407
Draine BT, McKee CF. 1993. *Ann. Rev. Astron. Astrophys.* 31:373–432
Draine BT, Roberge WG, Dalgarno A. 1983. *Astrophys. J.* 264:485–507
Dubernet ML, Alexander MH, Ba YA, Balakrishnan N, Balança C, et al. 2013. *Astron. Astrophys.* 553:A50
Dulieu F, Congiu E, Noble J, Baouche S, Chaabouni H, et al. 2013. *Scientific Reports* 3:1338
Eddington AS. 1926. *Royal Society of London Proceedings Series A* 111:424–456
Elitzur M, Hollenbach DJ, McKee CF. 1989. *Astrophys. J.* 346:983–990
Ewen HI, Purcell EM. 1951. *Nature* 168:356
Falgarone E, Godard B, Zwaan M, Andreani P. 2015. . In *Revolution in Astronomy with ALMA: The third year*, eds. D Iono, K Tatematsu, A Wootten, L Testi
Falgarone E, Phillips TG, Pearson JC. 2005. *Astrophys. J., Lett.* 634:L149–L152
Faure A, Crimier N, Ceccarelli C, Valiron P, Wiesenfeld L, Dubernet ML. 2007. *Astron. Astrophys.* 472:1029–1035
Faure A, Hily-Blant P, Le Gal R, Rist C, Pineau des Forêts G. 2013. *Astrophys. J., Lett.* 770:L2
Fedele D, Bruderer S, van Dishoeck EF, Carr J, Herczeg GJ, et al. 2013. *Astron. Astrophys.* 559:A77
Federman SR, Cardell JA, van Dishoeck EF, Lambert DL, Black JH. 1995. *Astrophys. J.* 445:325–329
Fedoseev G, Ioppolo S, Linnartz H. 2015. *MNRAS* 446:449–458
Feuchtgruber H, Helmich FP, van Dishoeck EF, Wright CM. 2000. *Astrophys. J., Lett.* 535:L111–L114
Field GB, Somerville WB, Dressler K. 1966. *Ann. Rev. Astron. Astrophys.* 4:207
Flagey N, Goldsmith PF, Lis DC, Gerin M, Neufeld D, et al. 2013. *Astrophys. J.* 762:11
Frail DA, Mitchell GF. 1998. *Astrophys. J.* 508:690–695
Fynbo JPU, Krühler T, Leighly K, Ledoux C, Vreeswijk PM, et al. 2014. *Astron. Astrophys.* 572:A12
Geballe TR, Oka T. 1996. *Nature* 384:334–335
Gerin M, de Luca M, Black J, Goicoechea JR, Herbst E, et al. 2010a. *Astron. Astrophys.* 518:L110
Gerin M, de Luca M, Goicoechea JR, Herbst E, Falgarone E, et al. 2010b. *Astron. Astrophys.* 521:L16
Gerin M, Levrier F, Falgarone E, Godard B, Hennebelle P, et al. 2012. *Royal Society of London Philosophical Transactions Series A* 370:5174–5185
Gerin M, Marcelino N, Biver N, Roueff E, Coudert LH, et al. 2009. *Astron. Astrophys.* 498:L9–L12
Glover SCO, Mac Low MM. 2007. *Astrophys. J.* 659:1317–1337
Godard B, Cernicharo J. 2013. *Astron. Astrophys.* 550:A8
Godard B, Falgarone E, Gerin M, Lis DC, De Luca M, et al. 2012. *Astron. Astrophys.* 540:A87
Godard B, Falgarone E, Pineau Des Forêts G. 2009. *Astron. Astrophys.* 495:847–867
Godard B, Falgarone E, Pineau des Forêts G. 2014. *Astron. Astrophys.* 570:A27
Goddi C, Zhang Q, Moscadelli L. 2015. *Astron. Astrophys.* 573:A108
Goicoechea JR, Chavarría L, Cernicharo J, Neufeld DA, Vavrek R, et al. 2015. *Astrophys. J.* 799:102
Goicoechea JR, Etxaluze M, Cernicharo J, Gerin M, Neufeld DA, et al. 2013. *Astrophys. J., Lett.* 769:L13
Goicoechea JR, Joblin C, Contursi A, Berné O, Cernicharo J, et al. 2011. *Astron. Astrophys.* 530:L16
Gómez-Carrasco S, Godard B, Lique F, Bulut N, Kłos J, et al. 2014. *Astrophys. J.* 794:33
González-Alfonso E, Fischer J, Bruderer S, Müller HSP, Graciá-Carpio J, et al. 2013. *Astron. Astrophys.* 550:A25
González-Alfonso E, Fischer J, Graciá-Carpio J, Sturm E, Hailey-Dunsheath S, et al. 2012. *Astron. Astrophys.*

541:A4
González-Alfonso E, Fischer J, Sturm E, Graciá-Carpio J, Veilleux S, et al. 2015. *Astrophys. J.* 800:69
Goto M, Usuda T, Geballe TR, Menten KM, Indriolo N, Neufeld DA. 2013. *Astron. Astrophys.* 558:L5
Gredel R. 1997. *Astron. Astrophys.* 320:929–944
Grenier IA, Casandjian JM, Terrier R. 2005. *Science* 307:1292–1295
Gusdorf A, Pineau Des Forêts G, Cabrit S, Flower DR. 2008. *Astron. Astrophys.* 490:695–706
Habart E, Dartois E, Abergel A, Baluteau JP, Naylor D, et al. 2010. *Astron. Astrophys.* 518:L116
Heays AN, Visser R, Gredel R, Ubachs W, Lewis BR, et al. 2014. *Astron. Astrophys.* 562:A61
Herbst E, Klemperer W. 1973. *Astrophys. J.* 185:505–534
Hierl PM, Morris RA, Viggiano AA. 1997. *JCP* 106:10145–10152
Hogerheijde MR, Bergin EA, Brinch C, Cleeves LI, Fogel JKJ, et al. 2011. *Science* 334:338–
Hollenbach D, Elitzur M, McKee CF. 2013. *Astrophys. J.* 773:70
Hollenbach D, Kaufman MJ, Bergin EA, Melnick GJ. 2009. *Astrophys. J.* 690:1497–1521
Hollenbach D, Kaufman MJ, Neufeld D, Wolfire M, Goicoechea JR. 2012. *Astrophys. J.* 754:105
Hollenbach DJ, Tielens AGGM. 1999. *Reviews of Modern Physics* 71:173–230
Hollenbach DJ, Werner MW, Salpeter EE. 1971. *Astrophys. J.* 163:165
Hollis JM, Jewell PR, Lovas FJ. 1995. *Astrophys. J.* 438:259–264
Honma M, Nagayama T, Ando K, Bushimata T, Choi YK, et al. 2012. *PASJ* 64:136
Indriolo N, McCall BJ. 2012. *Astrophys. J.* 745:91
Indriolo N, Neufeld DA, Gerin M, Schilke P, Benz AO, et al. 2015. *Astrophys. J.* 800:40
Indriolo N, Neufeld DA, Seifahrt A, Richter MJ. 2013. *Astrophys. J.* 764:188
Indriolo N, Oka T, Geballe TR, McCall BJ. 2010. *Astrophys. J.* 711:1338–1342
Jansen P, Bethlem HL, Ubachs W. 2014. *J. Chem. Phys.* 140:010901
Jiménez-Serra I, Caselli P, Martín-Pintado J, Hartquist TW. 2008. *Astron. Astrophys.* 482:549–559
Kama M, Caux E, López-Sepulcre A, Wakelam V, Dominik C, et al. 2015. *Astron. Astrophys.* 574:A107
Kamenetzky J, Glenn J, Rangwala N, Maloney P, Bradford M, et al. 2012. *Astrophys. J.* 753:70
Karska A, Kristensen LE, van Dishoeck EF, Drozdovskaya MN, Mottram JC, et al. 2014. *Astron. Astrophys.* 572:A9
Kaufman MJ, Neufeld DA. 1996. *Astrophys. J.* 456:611
Knez C, Lacy JH, Evans II NJ, van Dishoeck EF, Richter MJ. 2009. *Astrophys. J.* 696:471–483
Kramers HA, Ter Haar D. 1946. *BAIN* 10:137
Krełowski J, Beletsky Y, Galazutdinov GA. 2010. *Astrophys. J., Lett.* 719:L20–L22
Kulesa CA. 2002. *Molecular hydrogen and its ions in dark interstellar clouds and star forming regions*. Ph.D. thesis, THE UNIVERSITY OF ARIZONA
Lacy JH, Carr JS, Evans II NJ, Baas F, Achtermann JM, Arens JF. 1991. *Astrophys. J.* 376:556–560
Lacy JH, Knacke R, Geballe TR, Tokunaga AT. 1994. *Astrophys. J., Lett.* 428:L69–L72
Lanza M, Kalugina Y, Wiesenfeld L, Faure A, Lique F. 2014. *MNRAS* 443:3351–3358
Le Bourlot J. 2000. *Astron. Astrophys.* 360:656–662
Le Bourlot J, Le Petit F, Pinto C, Roueff E, Roy F. 2012. *Astron. Astrophys.* 541:A76
Le Gal R, Hily-Blant P, Faure A, Pineau des Forêts G, Rist C, Maret S. 2014. *Astron. Astrophys.* 562:A83
Li X, Arasa C, van Hemert MC, van Dishoeck EF. 2013. *Journal of Physical Chemistry A* 117:12889–12896
Lis DC, Neufeld DA, Phillips TG, Gerin M, Neri R. 2011. *Astrophys. J., Lett.* 738:L6
Lis DC, Phillips TG, Goldsmith PF, Neufeld DA, Herbst E, et al. 2010a. *Astron. Astrophys.* 521:L26
Lis DC, Schilke P, Bergin EA, Gerin M, Black JH, et al. 2014. *Astrophys. J.* 785:135
Lis DC, Wootten A, Gerin M, Roueff E. 2010b. *Astrophys. J., Lett.* 710:L49–L52
Liszt H, Lucas R. 1996. *Astron. Astrophys.* 314:917–926
Liszt H, Lucas R. 2002. *Astron. Astrophys.* 391:693–704
Lodders K. 2003. *Astrophys. J.* 591:1220–1247
Lucas R, Liszt H. 1996. *Astron. Astrophys.* 307:237
Lucas R, Liszt HS. 2000. *Astron. Astrophys.* 358:1069–1076
Luhman ML, Jaffe DT, Keller LD, Pak S. 1994. *Astrophys. J., Lett.* 436:L185–L188
Mattila K. 1986. *Astron. Astrophys.* 160:157–170

Melnick GJ, Menten KM, Phillips TG, Hunter T. 1993. *Astrophys. J., Lett.* 416:L37
Menten KM, Wyrowski F, Belloche A, Güsten R, Dedes L, Müller HSP. 2011. *Astron. Astrophys.* 525:A77
Merrill KM, Russell RW, Soifer BT. 1976. *Astrophys. J.* 207:763–769
Meyer DM, Roth KC. 1991. *Astrophys. J., Lett.* 376:L49–L52
Monje RR, Lis DC, Roueff E, Gerin M, De Luca M, et al. 2013. *Astrophys. J.* 767:81
Monje RR, Phillips TG, Peng R, Lis DC, Neufeld DA, Emprechtinger M. 2011. *Astrophys. J., Lett.* 742:L21
Muller S, Black JH, Guélin M, Henkel C, Combes F, et al. 2014a. *Astron. Astrophys.* 566:L6
Muller S, Combes F, Guélin M, Gérin M, Aalto S, et al. 2014b. *Astron. Astrophys.* 566:A112
Myers AT, McKee CF, Li PS. 2015. *MNRAS* 453:2747–2758
Nagy Z, Van der Tak FFS, Ossenkopf V, Gerin M, Le Petit F, et al. 2013. *Astron. Astrophys.* 550:A96
Neill JL, Wang S, Bergin EA, Crockett NR, Favre C, et al. 2013. *Astrophys. J.* 770:142
Neufeld DA. 2010. *Astrophys. J.* 708:635–644
Neufeld DA, Black JH, Gerin M, Goicoechea JR, Goldsmith PF, et al. 2015a. *Astrophys. J.* 807:54
Neufeld DA, Godard B, Gerin M, Pineau des Forêts G, Bernier C, et al. 2015b. *Astron. Astrophys.* 577:A49
Neufeld DA, Goicoechea JR, Sonnentrucker P, Black JH, Pearson J, et al. 2010. *Astron. Astrophys.* 521:L10
Neufeld DA, Gusdorf A, Güsten R, Herczeg GJ, Kristensen L, et al. 2014. *Astrophys. J.* 781:102
Neufeld DA, Roueff E, Snell RL, Lis D, Benz AO, et al. 2012. *Astrophys. J.* 748:37
Neufeld DA, Wolfire MG. 2009. *Astrophys. J.* 706:1594–1604
Neufeld DA, Wu Y, Kraus A, Menten KM, Tolls V, et al. 2013. *Astrophys. J.* 769:48
Neufeld DA, Zmuidzinas J, Schilke P, Phillips TG. 1997. *Astrophys. J., Lett.* 488:L141–L144
Öberg KI, Boogert ACA, Pontoppidan KM, Blake GA, Evans NJ, et al. 2008. *Astrophys. J.* 678:1032–1041
Oka T, Welty DE, Johnson S, York DG, Dahlstrom J, Hobbs LM. 2013. *Astrophys. J.* 773:42
Omont A, Yang C, Cox P, Neri R, Beelen A, et al. 2013. *Astron. Astrophys.* 551:A115
Ossenkopf V, Müller HSP, Lis DC, Schilke P, Bell TA, et al. 2010. *Astron. Astrophys.* 518:L111
Pagani L, Roueff E, Lesaffre P. 2011. *Astrophys. J., Lett.* 739:L35
Parise B, Du F, Liu FC, Belloche A, Wiesemeyer H, et al. 2012. *Astron. Astrophys.* 542:L5
Peng R, Yoshida H, Chamberlin RA, Phillips TG, Lis DC, Gerin M. 2010. *Astrophys. J.* 723:218–228
Persson C, OLofsson A, Le Gal R, Wirström E, Hassel G, Herbst E. 2015. *Astron. Astrophys.*
Persson CM, Black JH, Cernicharo J, Goicoechea JR, Hassel GE, et al. 2010. *Astron. Astrophys.* 521:L45
Persson CM, De Luca M, Mookerjea B, Olofsson AOH, Black JH, et al. 2012. *Astron. Astrophys.* 543:A145
Phillips TG, van Dishoeck EF, Keene J. 1992. *Astrophys. J.* 399:533–550
Pilleri P, Fuente A, Cernicharo J, Ossenkopf V, Berné O, et al. 2012. *Astron. Astrophys.* 544:A110
Pineau des Forêts G, Flower DR, Hartquist TW, Dalgarno A. 1986. *MNRAS* 220:801–824
Pineau des Forêts G, Roueff E, Flower DR. 1986. *MNRAS* 223:743–756
Polehampton ET, Menten KM, Brünken S, Winnewisser G, Baluteau JP. 2005. *Astron. Astrophys.* 431:203–213
Porras AJ, Federman SR, Welty DE, Ritchey AM. 2014. *Astrophys. J., Lett.* 781:L8
Prasad SS, Tarafdar SP. 1983. *Astrophys. J.* 267:603–609
Rachford BL, Snow TP, Destree JD, Ross TL, Ferlet R, et al. 2009. *Astrophys. J. Suppl.* 180:125–137
Rachford BL, Snow TP, Ross TL. 2014. *Astrophys. J.* 786:159
Rangwala N, Maloney PR, Glenn J, Wilson CD, Kamenetzky J, et al. 2014. *Astrophys. J.* 788:147
Rangwala N, Maloney PR, Glenn J, Wilson CD, Rykala A, et al. 2011. *Astrophys. J.* 743:94
Reid MJ, Menten KM, Zheng XW, Brunthaler A, Moscadelli L, et al. 2009. *Astrophys. J.* 700:137–148
Rist C, Faure A, Hily-Blant P, Le Gal R. 2013. *Journal of Physical Chemistry A* 117:9800–9806
Ritchey AM, Welty DE, Dahlstrom JA, York DG. 2015. *Astrophys. J.* 799:197
Roueff E, Gerin M, Lis DC, Wootten A, Marcelino N, et al. 2013. *Journal of Physical Chemistry A* 117:9959–9967
Roueff E, Lique F. 2013. *Chemical Reviews* 113:8906–8938
Roueff E, Lis DC, van der Tak FFS, Gerin M, Goldsmith PF. 2005. *Astron. Astrophys.* 438:585–598
Roueff E, Loison JC, Hickson KM. 2015. *Astron. Astrophys.* 576:A99
Sakai N, Maezawa H, Sakai T, Menten KM, Yamamoto S. 2012. *Astron. Astrophys.* 546:A103
Salyk C, Pontoppidan KM, Blake GA, Lahuis F, van Dishoeck EF, Evans II NJ. 2008. *Astrophys. J., Lett.* 676:L49–L52

Schilke P, Neufeld DA, Müller HSP, Comito C, Bergin EA, et al. 2014. *Astron. Astrophys.* 566:A29
Schöier FL, van der Tak FFS, van Dishoeck EF, Black JH. 2005. *Astron. Astrophys.* 432:369–379
Sheffer Y, Rogers M, Federman SR, Abel NP, Gredel R, et al. 2008. *Astrophys. J.* 687:1075–1106
Sipilä O, Caselli P, Harju J. 2015. *Astron. Astrophys.* 578:A55
Snow TP, McCall BJ. 2006. *Ann. Rev. Astron. Astrophys.* 44:367–414
Snow Jr. TP. 1976. *Astrophys. J., Lett.* 204:L127–L130
Solomon PM, Klemperer W. 1972. *Astrophys. J.* 178:389–422
Sonnentrucker P, Neufeld DA, Phillips TG, Gerin M, Lis DC, et al. 2010. *Astron. Astrophys.* 521:L12
Sonnentrucker P, Wolfire M, Neufeld DA, Flagey N, Gerin M, et al. 2015. *Astrophys. J.* 806:49
Spilker JS, Marrone DP, Aguirre JE, Aravena M, Ashby MLN, et al. 2014. *Astrophys. J.* 785:149
Spitzer L, Drake JF, Jenkins EB, Morton DC, Rogerson JB, York DG. 1973. *Astrophys. J., Lett.* 181:L116
Stäuber P, Doty SD, van Dishoeck EF, Benz AO. 2005. *Astron. Astrophys.* 440:949–966
Sternberg A, Dalgarno A. 1995. *Astrophys. J. Suppl.* 99:565
Sturm E, González-Alfonso E, Veilleux S, Fischer J, Graciá-Carpio J, et al. 2011. *Astrophys. J., Lett.* 733:L16
Sultanov RA, Balakrishnan N. 2005. *Astrophys. J.* 629:305–310
Swings P, Rosenfeld L. 1937. *Astrophys. J.* 86:483–486
Tappe A, Lada CJ, Black JH, Muench AA. 2008. *Astrophys. J., Lett.* 680:L117–L120
Thaddeus P, Kutner ML, Penzias AA, Wilson RW, Jefferts KB. 1972. *Astrophys. J., Lett.* 176:L73
Thi WF, Ménard F, Meeus G, Martin-Zaïdi C, Woitke P, et al. 2011. *Astron. Astrophys.* 530:L2
Tizniti M, Le Picard SD, Lique F, Berteloite C, Canosa A, et al. 2014. *Nature Chemistry* 6:141–145
Townes CH. 1957. *Microwave and radio-frequency resonance lines of interest to radio astronomy*. In *Radio astronomy*, ed. HC de Hulst, vol. 4 of *IAU Symposium*
van der Tak FFS, Nagy Z, Ossenkopf V, Makai Z, Black JH, et al. 2013. *Astron. Astrophys.* 560:A95
van der Tak FFS, Ossenkopf V, Nagy Z, Faure A, Röllig M, Bergin EA. 2012. *Astron. Astrophys.* 537:L10
van der Werf PP, Isaak KG, Meijerink R, Spaans M, Rykala A, et al. 2010. *Astron. Astrophys.* 518:L42
van Dishoeck EF. 1998. *The Molecular Astrophysics of Stars and Galaxies, edited by Thomas W. Hartquist and David A. Williams. Clarendon Press, Oxford, 1998., p.53* 4:53
van Dishoeck EF, Blake GA, Jansen DJ, Groesbeck TD. 1995. *Astrophys. J.* 447:760
van Dishoeck EF, Herbst E, Neufeld DA. 2013. *Chemical Reviews* 113:9043–9085
van Dishoeck EF, Jansen DJ, Schilke P, Phillips TG. 1993. *Astrophys. J., Lett.* 416:L83
Vastel C, Ceccarelli C, Caux E, Coutens A, Cernicharo J, et al. 2010. *Astron. Astrophys.* 521:L31
Vastel C, Phillips TG, Ceccarelli C, Pearson J. 2003. *Astrophys. J., Lett.* 593:L97–L100
Vigren E, Zhaunerchyk V, Hamberg M, Kaminska M, Semaniak J, et al. 2012. *Astrophys. J.* 757:34
Wagenblast R, Williams DA, Millar TJ, Nejad LAM. 1993. *MNRAS* 260:420–424
Walmsley CM, Ungerechts H. 1983. *Astron. Astrophys.* 122:164–170
Wardle M, Yusef-Zadeh F. 2002. *Science* 296:2350–2354
Watson WD, Salpeter EE. 1972. *Astrophys. J.* 174:321
Weinreb S, Barrett AH, Meeks ML, Henry JC. 1963. *Nature* 200:829–831
Weiß A, De Breuck C, Marrone DP, Vieira JD, Aguirre JE, et al. 2013. *Astrophys. J.* 767:88
Weiß A, Requena-Torres MA, Güsten R, García-Burillo S, Harris AI, et al. 2010. *Astron. Astrophys.* 521:L1
Weliachew L. 1971. *Astrophys. J., Lett.* 167:L47
Welty DE, Federman SR, Gredel R, Thorburn JA, Lambert DL. 2006. *Astrophys. J. Suppl.* 165:138–172
Whittet DCB, Poteet CA, Chiar JE, Pagani L, Bajaj VM, et al. 2013. *Astrophys. J.* 774:102
Wiesemeyer H, Güsten R, Heymick S, Hübers HW, Menten KM, et al. 2015. *Astron. Astrophys.*
Wirström ES, Charnley SB, Cordiner MA, Milam SN. 2012. *Astrophys. J., Lett.* 757:L11
Wolfire MG, Hollenbach D, McKee CF. 2010. *Astrophys. J.* 716:1191–1207
Wright CM, van Dishoeck EF, Cox P, Sidher SD, Kessler MF. 1999. *Astrophys. J., Lett.* 515:L29–L33
Wyrowski F, Menten KM, Güsten R, Belloche A. 2010. *Astron. Astrophys.* 518:A26
Yang C, Gao Y, Omont A, Liu D, Isaak KG, et al. 2013. *Astrophys. J., Lett.* 771:L24
Zanchet A, Agúndez M, Herrero VJ, Aguado A, Roncero O. 2013a. *Astron. Journal* 146:125
Zanchet A, Godard B, Bulut N, Roncero O, Halvick P, Cernicharo J. 2013b. *Astrophys. J.* 766:80

Related resources: On line services

1. The astrochymist (http://www.astrochymist.org) provides the list of detected molecules in the interstellar medium with the associated bibliographic references and related resources in astrochemistry.
2. BASECOL, a database devoted to collisional ro-vibrational excitation of molecules by colliders such as atom, ion, molecule or electron. http://basecol.obspm.fr/
3. Leiden Atomic and Molecular Database (LAMDA), a data base providing the basic atomic and molecular data for molecular excitation calculations. http://home.strw.leidenuniv.nl/ moldata/
4. Virtual Atomic and Molecular Data Centre (VAMDC). A portal for 28 databases providing atomic and molecular data. http://portal.vamdc.org/vamdc_portal/home.seam
5. The Cologne Database for Molecular Spectroscopy (CDMS). A molecular line catalog providing line frequencies, intensities and molecule partition functions. https://www.astro.uni-koeln.de/cdms
6. JPL molecular spectroscopy. A molecular line catalog providing line frequencies, intensities and molecule partition functions http://spec.jpl.nasa.gov/
7. Splatalogue, a portal to molecular spectroscopy databases. http://www.cv.nrao.edu/php/splat/
8. KInetic Database for Astrochemistry (KIDA). A data base of kinetic data. KIDA provides recommendations for a set of important chemical reactions. http://kida.obs.u-bordeaux1.fr/
9. The UMIST Database for Astrochemistry. a data base of kinetic data. UDFA http://udfa.ajmarkwick.net/
10. The ISM platform provides access to numerical codes and data bases of model results, notably the Meudon PDR code and Paris-Durham shock model. http://ism.obspm.fr